

Quantum Batteries in two-dimensional material-based Josephson Junctions

V. Varrica ^{1,2}, G. Gemme ^{3,4}, F.M.D. Pellegrino ^{1,2}, E. Paladino ^{1,2}, M. Sassetti^{3,4}, and D. Ferraro ^{3,4}

¹Dipartimento di Fisica e Astronomia "Ettore Majorana", Università di Catania, Via S. Sofia 64, I-95123 Catania, Italy

²INFN, Sez. Catania, I-95123 Catania, Italy

³Dipartimento di Fisica, Università di Genova, Via Dodecaneso 33, I-16146 Genova, Italy

⁴CNR-SPIN, Via Dodecaneso 33, I-16146 Genova, Italy

Abstract

We investigate the solid-state implementation of a Dicke-like quantum battery consisting of a two-dimensional material-based Josephson junction inductively coupled to a resonator, using graphene as a representative example. In this configuration, Andreev bound states naturally act as non-interacting, energetically non-degenerate two-level systems, and the setup allows for both single-photon and two-photon resonant processes. The coupling between the LC-circuit flux and the supercurrent through the junction gives rise to peculiar longitudinal interaction terms that have no counterpart in the conventional Dicke model. These additional couplings can enhance energy storage for a proper range of parameters. The proposed architecture also enables an alternative, but equivalent, charging protocol that relies on tuning the superconducting phase difference across the junction.

1 Introduction

Quantum batteries (QBs) are miniaturized devices able to efficiently store, transfer, and release energy on-demand by exploiting purely quantum effects [1–5]. They are progressively assuming a prominent role in the domain of quantum technologies [6] and in the emerging field of quantum energy [7]. Their main aim is to provide an energy supply to quantum devices and quantum sensors supporting their increasing complexity [8, 9].

The first theoretical proposals of QBs were based on a collection of independent two-level systems (TLSs) [10, 11]. Starting from these seminal works the field rapidly evolved, addressing a plethora of diverse platforms such as quantum spin chains [12–19], nuclear spins [20, 21], collisional models [22–27], superconducting circuits [28–31] and quantum harmonic oscillators [32–34]. Within this extremely varied context, probably the most successful scheme proposed so far is based on the matter-radiation interaction described by the Dicke model [35, 36]. Here, a collection of independent TLSs composing the QB is embedded in a resonant cavity that acts as a charger [37–43]. The charging process then consists of destroying the photons and promoting a large majority of the TLSs from the ground to the excited state. These Dicke-QBs show a collective quantum advantage in the charging power [44, 45], which has been experimentally observed in molecular-based setups [46]. The latest developments in this direction have addressed two fundamental aspects with the aim of improving the performance of these devices at the level of charging and storage respectively: the optimization of charging protocols using reinforcement learning techniques [47–49] and the exploitation of the features of the energy spectrum of the molecules composing the QBs [50, 51].

Due to the important achievements realized in the domain of circuit quantum electrodynamics (cQED) [52, 53], where unconventional regimes of matter-radiation interaction can be addressed using superconducting circuits coupled with resonators acting as LC circuits, it seems natural to investigate possible implementations of Dicke-QBs also in these solid-state based platforms. In this direction,

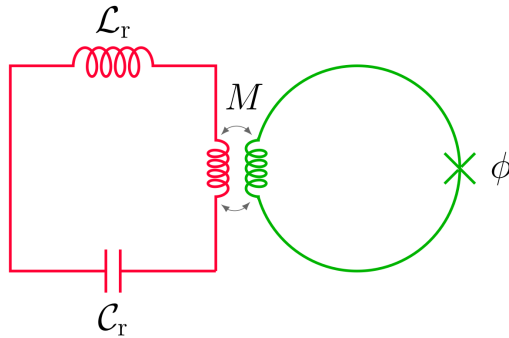


Figure 1: Scheme of a resonant circuit (red), described as a lumped-element LC circuit with an inductance \mathcal{L}_r and a capacitance \mathcal{C}_r , playing role of a quantum charger. This LC circuit is coupled, through a mutual inductance M , with a ring containing a single short JJ (green), which represents the QB. Here, ϕ is the superconducting phase difference between the two superconducting leads.

the present paper aims to explore a two-dimensional material-based Josephson junction inductively coupled with an LC circuit. Although the formalism applies to any planar JJ, the graphene Josephson junction (GJJ) has been selected as the representative case. Here, single- and two-photon Dicke-QB physics naturally emerge with Andreev bound states (ABSs) playing the role of non-interacting and energetically non-degenerate TLSs. Due to the presence of interaction between the LC-circuit flux and the supercurrent flowing through the junction, longitudinal couplings with no correspondence in the conventional Dicke model emerge. They lead to an enhancement of the energy storage associated with two-photon processes while influencing the dynamics of single-photon resonant processes. In view of actual experimental implementations, in this device, it is also possible to implement a charging protocol based on the modulation of the superconducting phase difference across the junction.

2 Model

We consider a device composed of a superconducting ring interrupted by a short superconductor-semiconductor Josephson Junction (JJ), which interacts via a mutual inductance M with a superconducting resonator, as shown in Fig. 1. In this cQED setup, the superconducting ring hosting the JJ (green) acts as the QB, while the superconducting resonator circuit (red) plays the role of the charger. Within this description, we are considering a charger-mediated protocol, in which the two quantum subsystems exchange energy through their mutual coupling, enabling the transfer of excitations between the charger and the QB [37, 41, 46].

In the limit of a short junction, when the physical length of the junction L is much smaller than the superconducting coherence length, $\xi \sim \hbar v_F / \Delta_0$, in the JJ, the flow of a supercurrent is microscopically sustained by pairs of ABSs, spatially confined in the normal phase region, which arise as a result of Andreev reflections occurring at the superconductor-semiconductor interfaces [54]. They are subgap states, namely eigenstates whose eigenenergies are symmetrically arranged around the Fermi level and have level spacing smaller than the superconducting energy gap $2\Delta_0$ [55]. Transport through JJ is also characterized by the total number of conduction channels N , which depends both on the microscopic properties of the semiconductor component and the geometry of the junction [56]. In the limit of a short junction, a single pair of ABSs is expected per conduction channel [57] with the eigenenergies $\pm \varepsilon_n(\phi)$ with

$$\varepsilon_n(\phi) = \Delta_0 \sqrt{1 - \tau_n \sin^2(\phi/2)}, \quad (1)$$

where \pm denotes if the ABS energy is above (+) or below (-) the Fermi level, τ_n is the transmission probability of the n -th conduction channel, and ϕ is the superconducting phase difference between the two superconducting leads of the junction. As a result, at zero temperature, each populated ABSs contributes to the current-phase relation (CPR) of the junction [58], which is given by

$$I(\phi) = -\frac{2e}{h} \sum_{n=1}^N \partial_\phi \varepsilon_n(\phi). \quad (2)$$

Within this description, the system of ABSs is represented as a collection of N non-interacting TLSs, characterized by different energy splittings $2\varepsilon_n(\phi)$. Specifically, for a given value of ϕ , by projecting the matter Hamiltonian in the low-energy subspace spanned by the ABSs [59], we can model the Hamiltonian of our QB system as

$$\hat{H}_B = \sum_{n=1}^N \varepsilon_n(\phi) \hat{\sigma}_n^z, \quad (3)$$

where $\hat{\sigma}_n^\beta$ ($\beta = x, y, z$) are the Pauli matrices associated with the 2×2 subspace spanned by the n -th pair of ABSs. In line with this, we define two more relevant eigenstates of the QB Hamiltonian in Eq (3), which are expressed as product states

$$|\downarrow\rangle = \otimes_{n=1}^N |\downarrow\rangle_n, \quad (4a)$$

$$|\uparrow\rangle = \otimes_{n=1}^N |\uparrow\rangle_n, \quad (4b)$$

where the first one is the ground state and the second one is the maximally excited eigenstate. Accordingly, the maximum amount of energy that can be stored by the QB, known as the energy storage capacity, reads

$$C_B(\phi) = \langle \uparrow | \hat{H}_B | \uparrow \rangle - \langle \downarrow | \hat{H}_B | \downarrow \rangle = 2 \sum_{n=1}^N \varepsilon_n(\phi). \quad (5)$$

It is worth noticing that the above quantity depends on the superconducting phase difference and can be tuned via the application of an external magnetic flux that threads the ring (green) shown in Fig. 1.

The auxiliary system, which plays the role of the charger, is a superconducting resonator (red) shown in Fig. 1. We model it as a lumped-element LC circuit with an inductance \mathcal{L}_r and a capacitance \mathcal{C}_r . Following the conventional quantization procedure [60], the Hamiltonian of the LC circuit reads

$$\hat{H}_r = \hbar\omega_r \left(\hat{a}^\dagger \hat{a} + \frac{1}{2} \right), \quad (6)$$

where \hat{a} (\hat{a}^\dagger) annihilates (creates) a photon of energy $\hbar\omega_r$, with $\omega_r = 1/\sqrt{\mathcal{L}_r \mathcal{C}_r}$. As outlined in previous works [61, 62], the interaction term describing the energy exchange between the two subsystems can be expressed in terms of a coupling g , which arises from the inductive interaction scheme assumed in the system and shown in Fig. 1. Within this picture, the total (charger+QB) Hamiltonian is obtained as a second-order expansion with respect to the coupling [63, 64] and reads

$$\hat{H} = \hat{H}_r + \hat{H}_B + g(\hat{a} + \hat{a}^\dagger) \sum_{n=1}^N \mathbf{P}_n \cdot \hat{\boldsymbol{\sigma}}_n + \frac{g^2}{2} (\hat{a} + \hat{a}^\dagger)^2 \sum_{n=1}^N \mathbf{D}_n \cdot \hat{\boldsymbol{\sigma}}_n, \quad (7)$$

where we introduced the short notations $\hat{\boldsymbol{\sigma}}_n = (\hat{\sigma}_n^z, \hat{\sigma}_n^x)^T$ and

$$\begin{aligned} \mathbf{P}_n &= (P_n^z(\phi), P_n^x(\phi))^T = \partial_\phi \varepsilon_n(\phi) \left(1, -\sqrt{1 - \tau_n} \tan\left(\frac{\phi}{2}\right) \right)^T, \\ \mathbf{D}_n &= (D_n^z(\phi), D_n^x(\phi))^T = \partial_\phi \varepsilon_n(\phi) \left(\frac{\tau_n + (2 - \tau_n) \cos(\phi)}{2 \sin(\phi)}, -\sqrt{1 - \tau_n} \right)^T, \end{aligned} \quad (8)$$

as vectors which encode the single-photon and two-photon coupling terms, respectively [65, 66]. Indeed, the third and fourth terms in Eq. (7) are analogous to the paramagnetic and diamagnetic contributions which typically emerge in the light-matter coupling Hamiltonian [67, 68].

Concerning the charging protocol, we follow what is usually proposed in the framework of Dicke QBs [9, 37, 46, 69], which consists of a sudden quench of the light-matter coupling. An alternative protocol implementable in the present setup will be discussed at the end of the paper. Consequently, we assume a time modulation of the inductive coupling in Eq. (7) in the form

$$g \rightarrow \bar{g}(t) = g\Theta(t)\Theta(t_c - t), \quad (9)$$

where $\Theta(t)$ is the Heaviside step function and t_c is a controllable charging time.

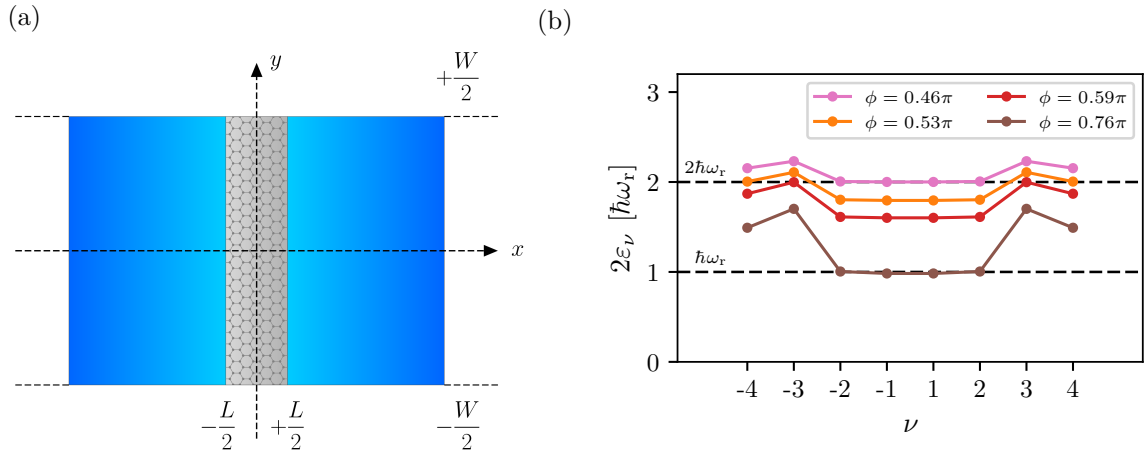


Figure 2: (a) Top view of a Josephson junction formed by graphene covered by two superconducting leads (blue). The uncovered grey region represents the graphene stripe in the normal phase. In this picture, L represents the junction channel length along the x -direction and W is the width of the device along the y -direction. (b) The energy splitting of each ABSs pair evaluated at $\phi/\pi = 0.46$ (pink), $\phi/\pi = 0.53$ (orange), $\phi/\pi = 0.59$ (red), $\phi/\pi = 0.76$ (brown). Horizontal dashed lines indicate the energies $\hbar\omega_r$ and $2\hbar\omega_r$, which make it possible to identify the units tuned to single-photon or two-photon resonance conditions, respectively. Here, the index $\nu = \zeta m$ is expressed using negative (positive) integers corresponding to the valley index $\zeta = -$ ($\zeta = +$), where m labels the associated wavevector q_m as defined in Eq. (12). Other parameters are $\hbar\omega_r = 0.75\Delta_0$, $\mu_0 = 6.5\hbar v_F/L$ and $W = 2L$.

In this work, we focus on the energy stored in the QB at a given time t as a figure of merit to characterize the performance of the device. It is defined as [69]

$$E_B^{(g)}(t) = \langle \psi(t) | \hat{H}_B | \psi(t) \rangle - \langle \psi(0) | \hat{H}_B | \psi(0) \rangle, \quad (10)$$

where $|\psi(0)\rangle$ denotes the initial state of the global system (see below), while $|\psi(t)\rangle$ represents the state at time $t \leq t_c$, which evolved according to the unitary generated by the Hamiltonian in Eq. (7).

In contrast to the conventional Dicke model [35, 36], which involves a set of identical TLSs, the QB considered here is composed of TLSs with a distribution of energy splittings and coupling strengths [70–72]. This has a deep impact on the symmetries of the system. More specifically, if we consider the collective pseudospin operators $\hat{S}_\beta = (\hbar/2) \sum_{n=1}^N \hat{\sigma}_n^\beta$, in our case we have that

$$[\hat{S}^2, \hat{H}(t)] \neq 0, \quad (11)$$

where $\hat{S}^2 = \hat{S}_x^2 + \hat{S}_y^2 + \hat{S}_z^2$. Therefore, we cannot take advantage of the block decomposition of the Dicke Hamiltonian based on the conservation of S^2 and the consequent reduction in computational cost. This leads us to investigate the behaviour of the QB, containing N ABSs, employing a fully numerical procedure which addresses the complete Hilbert space of the ABSs (matter) sector characterized by a dimension $d_m = 2^N$. In addition to this, although a rigorous treatment of the light sector would involve an infinite Hilbert space, we employ a truncated representation of dimension d_{ph} that accommodates a maximum of $4N$ excitations. We have set this as the dimension threshold after a comparison with the results obtained in the case with $d_{ph} + 1$, which confirmed that this dimension is large enough to guarantee an accurate convergence of the numerical results [37, 41].

3 Results

In this work, we consider a short planar graphene JJ (GJJ) characterized by a finite width W , as shown in Fig. 2(a). Here, the electronic properties of this device can be tuned by changing the Fermi level μ_0 . By exploiting the device spatial symmetry, it is natural to use the transverse momentum component to label the system eigenstates when solving the eigenvalue problem.

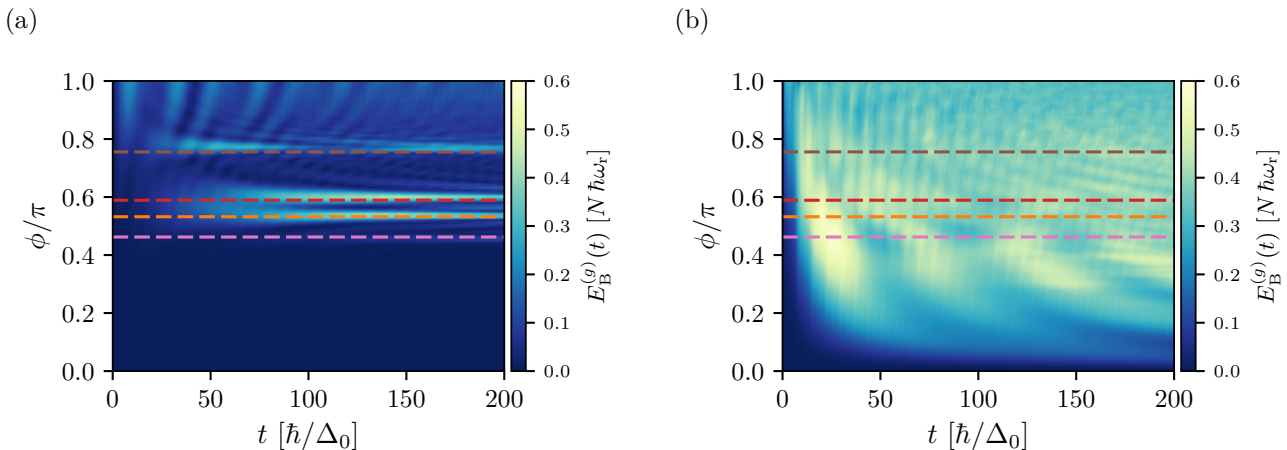


Figure 3: Energy $E_B^{(g)}$ stored in the QB system (in units of $N\hbar\omega_r$) as a function of the time and the superconducting phase difference ϕ , setting $g = 0.1$ (a) and $g = 0.3$ (b). In both panels, using the same scheme of colors used in Fig. 2(b), the dashed lines indicates the values of ϕ such that there are at least two pairs of ABSs which enable single-photon ($\phi = 0.76\pi$, brown), or two-photon resonant processes ($\phi = 0.46\pi$, pink), ($\phi = 0.53$, orange), and ($\phi = 0.59$ red). In all panels, the times are reported in units of \hbar/Δ_0 . Other parameters are $\hbar\omega_r = 0.75\Delta_0$, $\mu_0 = 6.5\hbar v_F/L$ and $W = 2L$.

Due to the finite width W , it is necessary to consider boundary conditions. Specifically, following Ref. [73], we apply the so-called infinite-mass boundary conditions for the $y = \{-W/2, +W/2\}$ transverse boundaries. As a result, the transverse wavevector k becomes quantized as

$$q_m = \frac{\pi L}{W} \left(m - \frac{1}{2} \right), \quad m = 1, 2, \dots, \quad (12)$$

where we multiplied the transverse wavevector by L , in order to express q_m in dimensionless form.

The short-junction regime, $L \ll \xi$, enables us to express the ABS eigenenergies in terms of the transmission probability within the normal-phase region [54]. In particular, for the GJJ under investigation, one has

$$\tau_m = \frac{(k_F^2 - q_m^2)}{[k_F^2 - q_m^2 \cos^2(\sqrt{k_F^2 - q_m^2})]}, \quad (13)$$

where $k_F = |\mu_0|L/\hbar v_F$ is the Fermi wavenumber in units of $1/L$ and $v_F \sim c/300$ is the Fermi velocity in graphene. As a result, the number of propagating modes, i.e., characterized by $q_m \leq k_F$, is given by $N_m = \lfloor \mu_0 W/\pi\hbar v_F + 1/2 \rfloor$ ($\lfloor \cdot \rfloor$ indicating the integer part). Notice that we have also taken into account the valley degree of freedom in graphene, $\zeta = \pm$, which introduces a double degeneracy in our model. Consequently, $N \equiv 2N_m$ is the total number of conduction channels responsible for transport in the GJJ, and they coincide with the number of units composing the QB. According to this, comparing with the Hamiltonian in Eq. (7), it is useful to replace the label n with a composite index $\nu \equiv \zeta m$.

From now on, we fix the Fermi level and the geometric aspect ratio to the values $\mu_0 = 6.5\hbar v_F/L$ and $W/L = 2$ respectively. This configuration corresponds to a QB system with $N = 8$, as shown in Fig. 2(b). Furthermore, the same Figure shows the dependence of the splitting energy of each ABSs pair on the superconducting phase difference across the junction, ϕ . In particular, we set the bare resonator energy at $\hbar\omega_r = 0.75\Delta_0$ and tune ϕ so that there are at least two pairs of ABSs fulfilling either the single-photon resonance condition $2\varepsilon_n(\phi) = \hbar\omega_r$ (shown in brown in Fig. 2(b)) or the two-photon resonance condition $2\varepsilon_n(\phi) = 2\hbar\omega_r$ (shown in pink, orange, and red in Fig. 2(b)). In what follows, we denote these cases as resonance conditions, whereby the two possible resonance processes occur selectively for at least two pairs of ABSs rather than for the entire ensemble.

We numerically investigate the time evolution of the stored energy $E_B^{(g)}$, defined in Eq. (10), by considering different fixed values of the superconducting phase difference ϕ . Here, we introduce the superscript (g) to indicate that the evolution is governed by the charging protocol defined in Eq. (9),

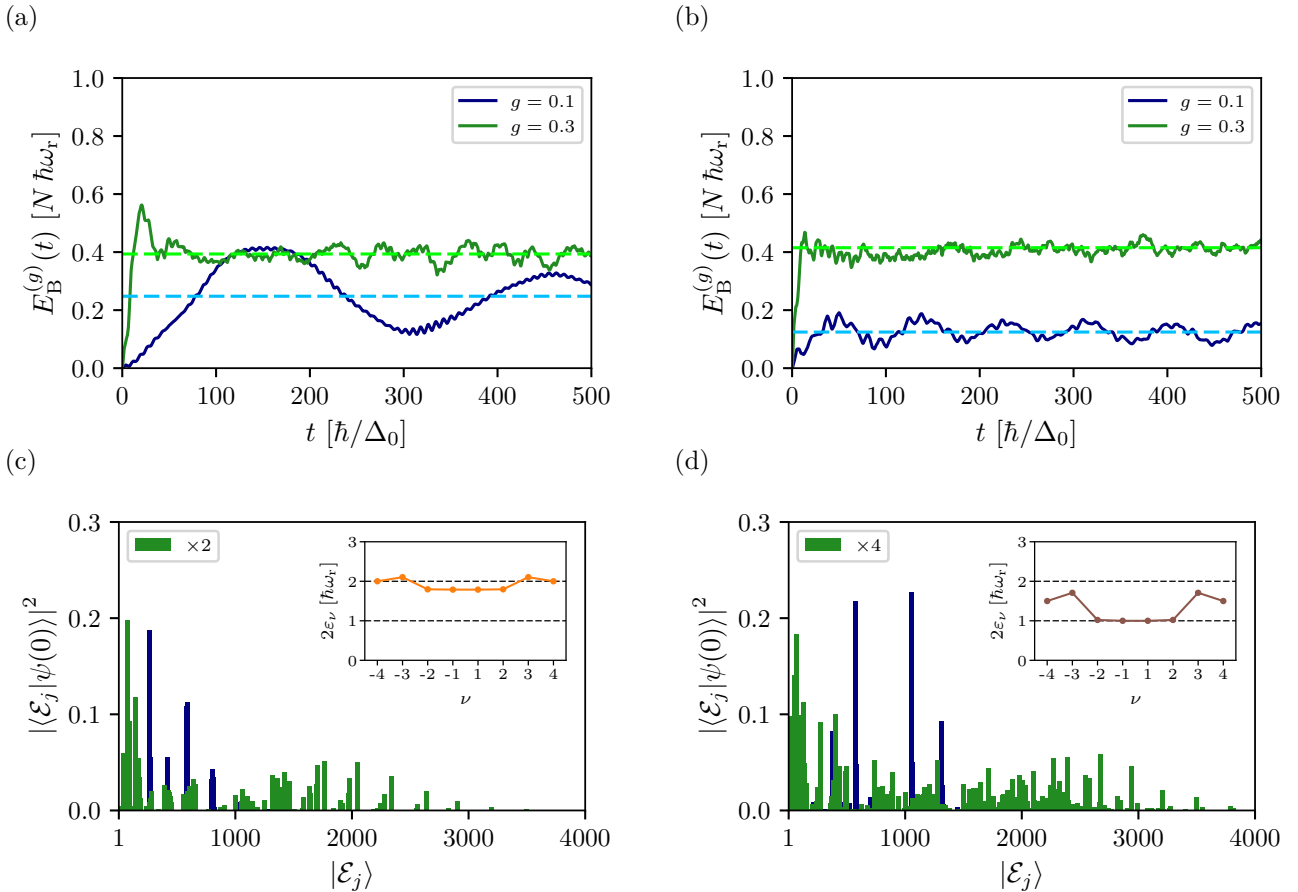


Figure 4: Long-time behaviour of $E_B^{(g)}$ (solid lines) evaluated at $\phi/\pi = 0.53$ (a) and at $\phi/\pi = 0.76$ (b). In both panels, time is expressed in units of \hbar/Δ_0 , and the stationary values $\bar{E}_B^{(g)}$ (dashed lines) are denoted in light green for $g = 0.1$ and in cyan for $g = 0.3$. (c)–(d) Bar plots illustrating the decomposition of the initial state $|\psi(0)\rangle$, over the relevant subset of the eigenbasis $\{|\mathcal{E}_j\rangle\}$, corresponding to the cases shown in (a)–(b). To improve graphical readability, the green bars in (c) and (d) are scaled by a factor 2 and 4, respectively. In the insets, the distribution of the ABSs energy splittings is shown (as in Fig. 2(b)). In all panels, we compare two values of the coupling constant: $g = 0.1$ (blue) and $g = 0.3$ (green). Other parameters are $\hbar\omega_r = 0.75\Delta_0$, $\mu_0 = 6.5\hbar v_F/L$ and $W = 2L$.

thus distinguishing it from the alternative charging protocol discussed below. In particular, the initial state is

$$|\psi(0)\rangle = |N\rangle \otimes |\downarrow\rangle, \quad (14)$$

which is a factorized state and describes the resonator in the Fock state with N photons and the QB in its ground state when the GJJ circuit is isolated, as defined in Eq. (4b). We note that, starting from $|\psi(0)\rangle$, even if all photons are absorbed simultaneously in single-photon processes, at most N distinct TLSs can be excited. Fig. 3 displays the time evolution of the stored energy for various values of ϕ , with the coupling constant fixed at $g = 0.1$ (a) and $g = 0.3$ (b). The stored energy is expressed in units of $N\hbar\omega_r$, corresponding to the initial energy supplied by the charger. Consequently, the ratio $E_B^{(g)}(t)/(N\hbar\omega_r)$ quantifies the fraction of energy transferred from the charger to the QB during the charging process. Fig. 3(a) shows particular values of ϕ at which the charging exhibits an enhancement. All these values of the superconducting phase difference correspond to situations where at least two pairs of units are in single-photon or two-photon resonance. However, the reverse is not always true: for instance, at $\phi = 0.46\pi$ (pink), there are two pairs of units in a two-photon resonance condition, but no clear enhancement of the charging is observed. This happens when the resonant units exhibit nearly perfect transmission, $\tau_n \lesssim 1$. Consequently, according to Eq. (8), their transverse couplings, $P_n^x(\phi)$ and $D_n^x(\phi)$, are strongly suppressed for superconducting phase differences far from $\phi = \pi$, thereby inhibiting

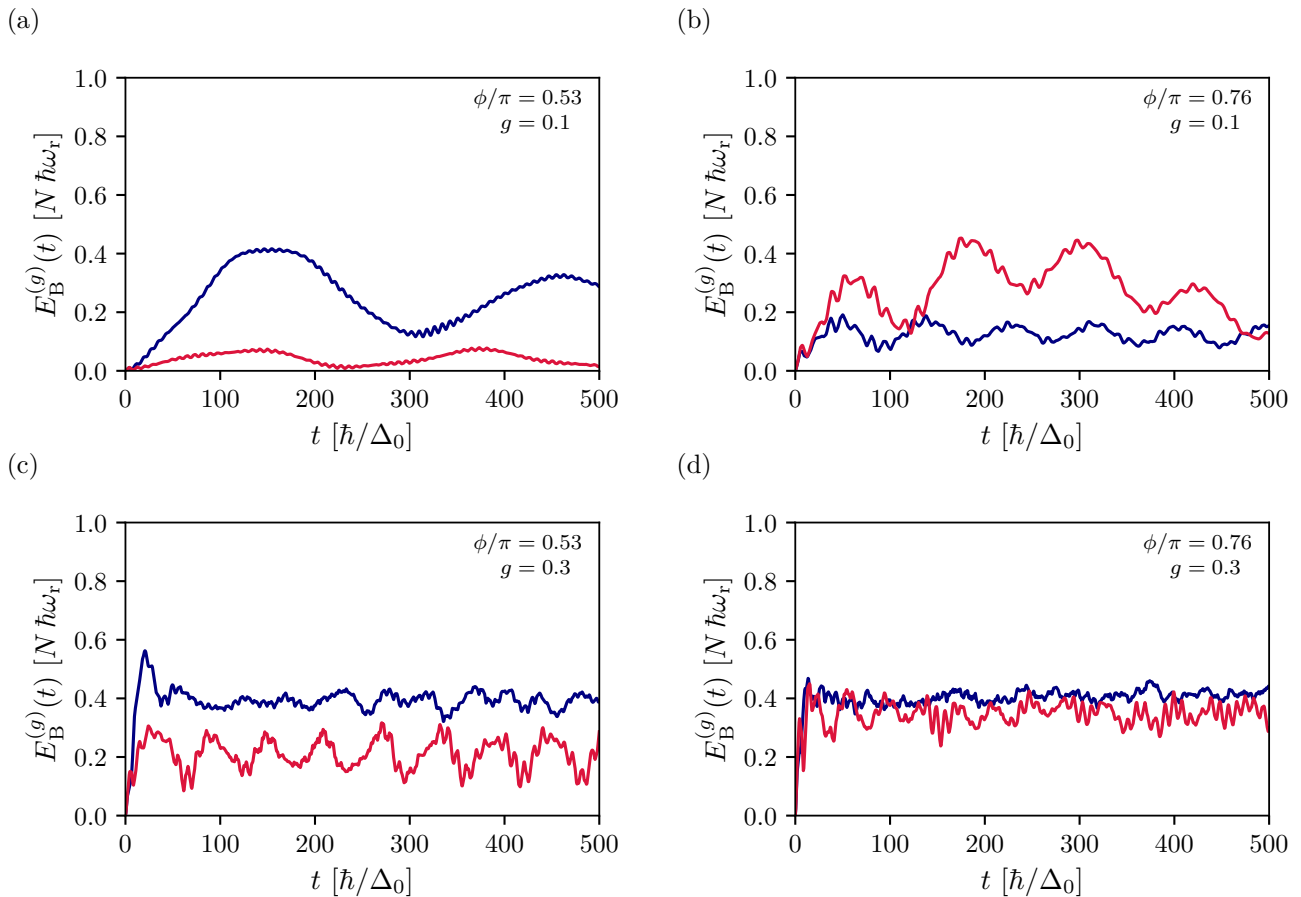


Figure 5: Comparison between the time evolution of the energy stored in the QB system (in units of $N\hbar\omega_r$) obtained according to the complete Hamiltonian in Eq. (7) (blue solid lines) and the corresponding results computed discarding the longitudinal terms at first order in g (red solid lines), i.e., the one proportional to $P_n^z(\phi)$. We show the results for $\phi/\pi = 0.53$ (a)–(c) and for $\phi/\pi = 0.76$ (b)–(d). In panels (a) and (b) we report the case with $g = 0.1$, while in the panels (c) and (d) we set $g = 0.3$. In all panels, the times are reported in units of \hbar/Δ_0 . Other parameters are $\hbar\omega_r = 0.75\Delta_0$, $\mu_0 = 6.5\hbar v_F/L$ and $W = 2L$.

the exchange of energy between the resonator and the QB system. Moreover, the largest stored energy, $E_B^{(g)}(t)/(N\hbar\omega_r) \simeq 40\%$, is reached when there is a subset of units of the QB system whose bare energy splittings are in a two-photon resonance condition at $\phi = 0.53\pi$ (orange dashed line). Conversely, in Fig. 3(b), the resonant processes cannot be distinguished as clearly. In this case, characterized by a larger value of the coupling, stored energies up to $E_B^{(g)}(t)/(N\hbar\omega_r) \simeq 60\%$ are generally reached at earlier times compared to the situation with $g = 0.1$, and larger values are spread more uniformly across extended regions. Nevertheless, the maximum stored energy occurs for a superconducting phase difference in the range $0.3\pi \lesssim \phi \lesssim 0.6\pi$, where two-photon resonant processes take place. In contrast to the $g = 0.1$ case, the corresponding charging peaks are not well separated here.

To further investigate the time evolution of the stored energy, we focus on the two representative cases $\phi = 0.53\pi$ (orange dashed line) and $\phi = 0.76\pi$ (brown dashed line), reported in Fig. 3, corresponding to a two-photon and single-photon resonance condition for some ABSs pairs, respectively. In the former case ($\phi = 0.53\pi$), represented in Fig. 4(a), the maximum stored energy achieved for $g = 0.1$ (blue solid line) is comparable to the values observed for $g = 0.3$ (green solid line). In contrast, in the second case ($\phi = 0.76\pi$) shown in Fig. 4(b), the stored energy corresponding to $g = 0.1$ (blue solid line) remains smaller than the one for $g = 0.3$ (green solid line) at all times. Moreover, in both reported cases, the long-term evolution of the stored energy exhibits a suppression of the oscillations, and its average value approaches a constant energy. To compute this average energy value, it is convenient to

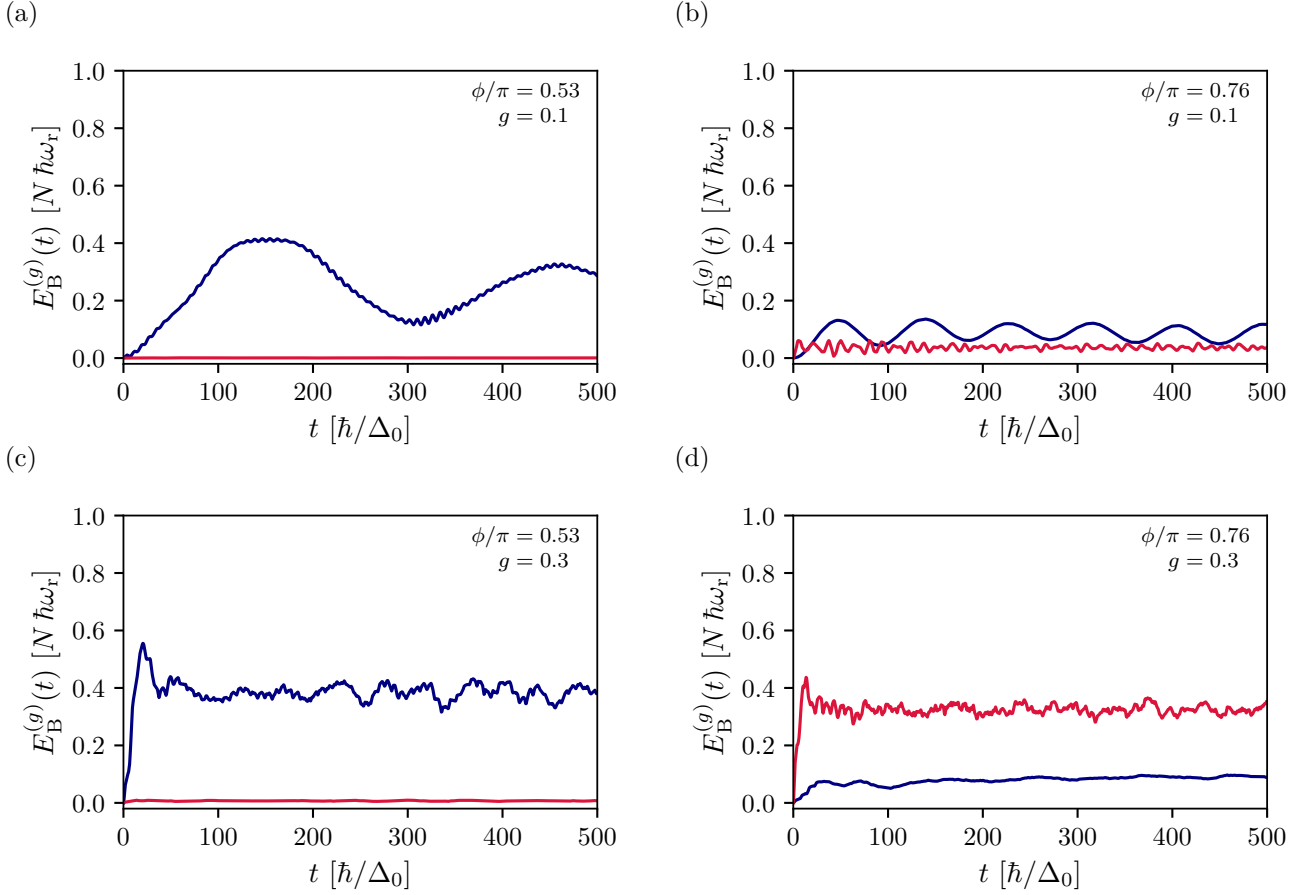


Figure 6: Time evolution of the energy stored in the QB system (expressed in units of $N\hbar\omega_r$), separated into a close resonant part (blue solid lines) and an off-resonant part (red solid lines), as defined in Eq. (17). In panels (a)–(c), we set $\phi/\pi = 0.53$ and have the subset of close resonant TLSs as $\mathcal{S} \equiv \{\nu = \pm 3, \pm 4\}$. In panels (b)–(d), we instead take $\phi/\pi = 0.76$, for which the close resonant TLSs are given by $\mathcal{S} \equiv \{\nu = \pm 1, \pm 2\}$. Panels (a) and (b) show the case with $g = 0.1$, whereas in panels (c) and (d) we take $g = 0.3$. In all panels, time is measured in units of \hbar/Δ_0 . The remaining parameters are $\hbar\omega_r = 0.75\Delta_0$, $\mu_0 = 6.5\hbar v_F/L$, and $W = 2L$.

decompose the evolving state that describes the system in the eigenbasis $\{|\mathcal{E}_j\rangle\}$ of the total Hamiltonian \hat{H} , defined in Eq. (7).

As a result, one obtains

$$E_B^{(g)}(t) = \sum_j |c_j|^2 \langle \mathcal{E}_j | \hat{H}_B | \mathcal{E}_j \rangle - \langle \psi(0) | \hat{H}_B | \psi(0) \rangle + \sum_{\ell \neq j} \sum_j e^{-i\Omega_{\ell j} t} c_\ell^* c_j \langle \mathcal{E}_\ell | \hat{H}_B | \mathcal{E}_j \rangle, \quad (15)$$

where $\Omega_{\ell j} = (\mathcal{E}_j - \mathcal{E}_\ell)/\hbar$ and $c_j = \langle \mathcal{E}_j | \psi(0) \rangle$ denotes the j -th component of the initial state in Eq. (14), obtained by projecting it onto the eigenbasis $\{|\mathcal{E}_j\rangle\}$, which is calculated via numerical diagonalization of \hat{H} .

It is straightforward to recognize that the time-independent component of $E_B^{(g)}(t)$ is given by

$$\bar{E}_B^{(g)} = \sum_j |c_j|^2 \langle \mathcal{E}_j | \hat{H}_B | \mathcal{E}_j \rangle - \langle \psi(0) | \hat{H}_B | \psi(0) \rangle. \quad (16)$$

In the cases shown in Figs. 4(a) and 4(b), the constant term introduced in Eq. (16) is represented as a dashed line, corresponding to $g = 0.1$ (cyan) and $g = 0.3$ (light green), respectively.

Here, for the smallest coupling constant, $g = 0.1$ (blue solid line), clear oscillations are observed, whereas for $g = 0.3$ the oscillations are less pronounced. This aligns with the expansion of $|\psi(0)\rangle$ in the eigenbasis $\{|\mathcal{E}_j\rangle\}$. In particular, Fig. 4(c) and Fig. 4(d) display the squared magnitudes of the

coefficients, $|c_j|^2 = |\langle \mathcal{E}_j | \psi(0) \rangle|^2$, for the chosen cases $\phi/\pi = 0.53$ and $\phi/\pi = 0.76$. For $g = 0.1$ (blue bars), the initial state can essentially be represented as a linear combination of only a small number of eigenstates of \hat{H} . Accordingly, in this case, the stored energy $E_B^{(g)}$ evolves in time as a function of only a limited set of frequencies $\Omega_{\ell j}$, which therefore appear clearly distinguishable. In contrast, for $g = 0.3$ (green bars), the distribution of the components of the eigenstates of \hat{H} is broader and poorly resolved, resulting in large frequencies $\Omega_{\ell j}$ involved in the dynamics. As a consequence, the time evolution of $E_B^{(g)}$ (green solid line), shown in Fig. 4(a) and Fig. 4(b), displays a rapidly oscillating behaviour. Furthermore, we observe that the timescale over which the energy profile $E_B^{(g)}(t)$ settles around the stationary component $\bar{E}_B^{(g)}(t)$ is reduced by approximately one order of magnitude compared to the $g = 0.1$ case (blue solid line).

We conclude this section by discussing the role played by the longitudinal term appearing at first order in g in Eq. (7), namely the one proportional to $P_n^z(\phi)$. Microscopically, this longitudinal term accounts for the equilibrium supercurrent carried by the occupied ABS through the JJ disconnected from the LC resonator, and there is no equivalent term in the conventional Dicke Hamiltonian [35, 36]. Here, we examine the numerically evaluated energy evolution for representative cases. Fig. 5 shows how the energy stored in the QB system evolves both in the presence (blue solid lines) and in the absence (red solid lines) of the terms $P_n^z(\phi)$.

From a comparison with the energy scheme in Fig. 2(b), we see that in the parameter regime reported in Fig. 5(a) there is a subset of TLSs, which we denote by \mathcal{S} , such that for $n \in \mathcal{S}$ one has $|2\hbar\omega_r - 2\varepsilon_n(\phi)| < \Delta_0/10$. In this situation, the charging process is expected to be predominantly governed by two-photon resonance processes. From the comparison between the curves in Fig. 5(a), it is clear that the terms $P_n^z(\phi)$ play a supporting role in the charging process. In Fig. 5(c), we keep the same phase difference but increase the coupling constant to $g = 0.3$. We again find that the terms $P_n^z(\phi)$ provide a positive contribution to energy storage.

In the case shown in Fig. 5(b), there is a subset of TLSs, again denoted by \mathcal{S} , such that for $n \in \mathcal{S}$ one has $|\hbar\omega_r - 2\varepsilon_n(\phi)| < \Delta_0/10$. Here, the charging process is expected to be predominantly governed by single-photon resonance processes. In this regime, we observe that the terms $P_n^z(\phi)$ act as a source of disturbance in the charging dynamics: removing this contribution from the Hamiltonian improves energy storage. Keeping the same phase difference but increasing the coupling constant to $g = 0.3$, Fig. 5(d) shows that the larger value of g modifies the influence of $P_n^z(\phi)$ on energy storage, resulting in a slightly supporting contribution.

To clarify the results discussed above, in Fig. 6 we analyze the representative cases by separating the contribution to the stored energy into that arising from the TLSs tuned in resonance or near-resonance, which define the subset \mathcal{S} , and that coming from the remaining TLSs. Formally, we decompose the stored energy as

$$E_B^{(g)}(t) = E_B^{(g)\text{-I}}(t) + E_B^{(g)\text{-II}}(t), \quad (17a)$$

$$E_B^{(g)\text{-I}}(t) = \sum_{n \in \mathcal{S}} \varepsilon_n(\phi) [\langle \psi(t) | \hat{\sigma}_n^z | \psi(t) \rangle - \langle \psi(0) | \hat{\sigma}_n^z | \psi(0) \rangle], \quad (17b)$$

$$E_B^{(g)\text{-II}}(t) = \sum_{n \notin \mathcal{S}} \varepsilon_n(\phi) [\langle \psi(t) | \hat{\sigma}_n^z | \psi(t) \rangle - \langle \psi(0) | \hat{\sigma}_n^z | \psi(0) \rangle]. \quad (17c)$$

Here, as indicated, $E_B^{(g)\text{-I}}(t)$ (blue solid lines) represents the close resonant contribution, corresponding to the energy stored in the TLSs belonging to \mathcal{S} , while $E_B^{(g)\text{-II}}(t)$ (red solid lines) represents the off-resonant contribution, associated with all the remaining TLSs. In the case $\phi/\pi = 0.53$, there is a subset \mathcal{S} of TLSs that satisfy, or are close to satisfying, the two-photon resonance condition. In this regime, we observe that the close resonant contribution $E_B^{(g)\text{-I}}(t)$ overwhelmingly dominates over $E_B^{(g)\text{-II}}(t)$. This indicates that, in this parameter regime, the charging processes can be effectively described in terms of two-photon resonant processes over a broad range of g values. Otherwise, when the phase difference is fixed at $\phi/\pi = 0.76$, there exists a subset \mathcal{S} of TLSs that satisfy single-photon resonance or are close to it. In this regime, the close resonant contribution $E_B^{(g)\text{-I}}(t)$ is slightly larger than the remaining contribution $E_B^{(g)\text{-II}}(t)$ for $g = 0.1$. However, when the coupling increases to $g = 0.3$, the off-resonant contribution becomes dominant. This shows that in this parameter range the charging dynamics can

be accurately captured in terms of single-photon resonant processes only for sufficiently small couplings $g \ll 1$.

To further analyze these representative cases, we perform a perturbative analysis. Although this method is approximate, it allows us to obtain qualitative insight for the interpretation of the numerical results. For convenience, we work in the interaction picture [74], where the total Hamiltonian can be written as

$$\tilde{H}(t) = \tilde{H}_0 + \tilde{V}(t) , \quad (18)$$

with

$$\tilde{H}_0 = \hat{H}_r + \hat{H}_B , \quad (19a)$$

$$\tilde{V}(t) = \tilde{V}_1(t) + \tilde{V}_2(t) , \quad (19b)$$

$$\tilde{V}_1(t) = \bar{g}(t)(\hat{a}e^{-i\omega_r t} + \hat{a}^\dagger e^{i\omega_r t}) \sum_{n=1}^N \left[P_n^z \hat{\sigma}_n^z + P_n^x \left(\hat{\sigma}_n^- e^{-i2\varepsilon_n(\phi)t/\hbar} + \hat{\sigma}_n^+ e^{i2\varepsilon_n(\phi)t/\hbar} \right) \right] , \quad (19c)$$

$$\tilde{V}_2(t) = \frac{\bar{g}(t)^2}{2} (\hat{a}e^{-i\omega_r t} + \hat{a}^\dagger e^{i\omega_r t})^2 \sum_{n=1}^N \left[D_n^z \hat{\sigma}_n^z + D_n^x \left(\hat{\sigma}_n^- e^{-i2\varepsilon_n(\phi)t/\hbar} + \hat{\sigma}_n^+ e^{i2\varepsilon_n(\phi)t/\hbar} \right) \right] . \quad (19d)$$

Using the time-dependent perturbation theory up to second order in g , the state of the system can be written as

$$|\tilde{\psi}(t)\rangle \approx |\tilde{\psi}^{(0)}\rangle + |\tilde{\psi}^{(1)}(t)\rangle + |\tilde{\psi}^{(2)}(t)\rangle , \quad (20)$$

where

$$|\tilde{\psi}^{(0)}\rangle = |\psi(0)\rangle , \quad (21a)$$

$$|\tilde{\psi}^{(1)}(t)\rangle = \int_0^t \frac{dt_1}{i\hbar} \tilde{V}_1(t_1) |\psi(0)\rangle , \quad (21b)$$

$$|\tilde{\psi}^{(2)}(t)\rangle = \int_0^t \frac{dt_1}{i\hbar} \left[\tilde{V}_2(t_1) + \tilde{V}_1(t_1) \int_0^{t_1} \frac{dt_2}{i\hbar} \tilde{V}_1(t_2) \right] |\psi(0)\rangle . \quad (21c)$$

We now identify the perturbative contributions that are most relevant for the charging dynamics. The first-order correction contains terms of the form $\hat{a}\sigma_n^+$ and $\hat{a}^\dagger\sigma_n^-$, each weighted by a factor $P_n^x(\phi)$. These correspond to single-photon resonant processes, which in the rotating frame evolve with the detuning $\omega_r - 2\varepsilon_n(\phi)/\hbar$. Exactly at the single-photon resonance, these terms become time-independent and play a key role in the charging dynamics when a subset \mathcal{S} of TLSs satisfies $|\hbar\omega_r - 2\varepsilon_n(\phi)| < \Delta_0/10$. These terms are also present in the conventional Dicke model [37], and the presence of the terms $P_n^z(\phi)$ does not introduce an additional single-photon resonant mechanism. The second-order correction contains terms $\hat{a}^2\sigma_n^+$ and $\hat{a}^{\dagger 2}\sigma_n^-$, weighted by D_n^x , corresponding to two-photon resonant processes with detuning $2[\omega_r - \varepsilon_n(\phi)/\hbar]$. Exactly at the two-photon resonance condition, these contributions become time-independent. The presence of terms $P_n^z(\phi)$ together with $P_m^x(\phi)$ generates additional terms of the form $\hat{a}^2\sigma_m^+\sigma_n^z$ and $\hat{a}^{\dagger 2}\sigma_m^-\sigma_n^z$, each weighted by $P_m^x(\phi)P_n^z(\phi)$, representing further resonant two-photon mechanisms.

Moreover, the terms $P_n^z(\phi)$ generate time-independent contributions of order g^2 . In particular, terms of the form $(2\hat{a}^\dagger\hat{a} + 1)\hat{\sigma}_n^z\hat{\sigma}_m^z$, weighted by $P_n^z(\phi)P_m^z(\phi)$ with $n, m = 1, \dots, N$, appear and correspond to N^2 photon-mediated longitudinal couplings between ABSs. In addition, \tilde{V}_2 produces N terms of the type $(2\hat{a}^\dagger\hat{a} + 1)\hat{\sigma}_n^z$, weighted by $D_n^z(\phi)$. During the charging process, these contributions of order g^2 lead to effective state-dependent energies $\varepsilon_n(\phi) + g^2\Xi_n(t)$, where $\Xi_n(t)$ depends on quantities such as $\langle\hat{a}^\dagger\hat{a}\rangle$ and $\langle\hat{\sigma}_m^z\rangle$. As a consequence, the detuning becomes dynamically renormalized during the charging process. An ensemble of TLSs that is initially tuned to the single-photon or two-photon resonance condition can therefore be shifted out of resonance as the photon population and ABS occupations evolve, thus hampering the charging dynamics.

In summary, when a subset of TLSs is tuned to a two-photon resonance, the terms $P_n^z(\phi)$ have a beneficial effect because it generates additional resonant processes. By contrast, when the system is tuned to a single-photon resonance, the terms $P_n^z(\phi)$ do not produce additional resonant contributions.

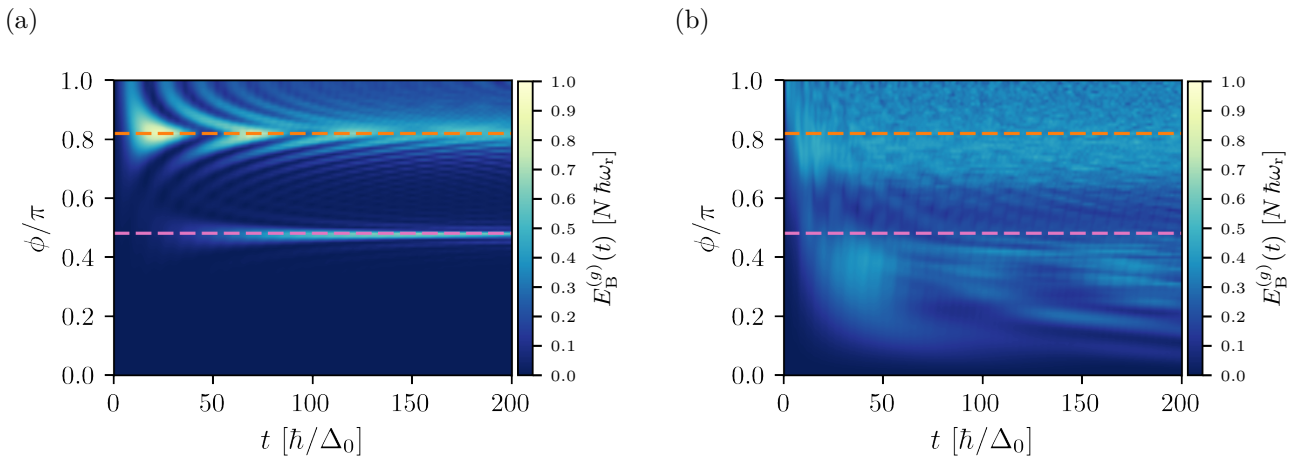


Figure 7: Time evolution of the energy stored in the QB system (in units of $N\hbar\omega_r$), evaluated for $g = 0.1$ (a) and $g = 0.3$ (b) as a function of the superconducting phase difference ϕ . The two values of the superconducting phase difference $\phi/\pi = 0.82$ (orange dashed line) and $\phi/\pi = 0.48$ (pink dashed line) correspond to single-photon and double-photon resonance conditions, respectively. In all panels, the times are reported in units of \hbar/Δ_0 . Other parameters are $\tau_{\text{eff}} = 0.93$, $N = 8$, $\hbar\omega_r = 0.75\Delta_0$.

Its dominant effect is, instead, to induce a time-dependent detuning, which tends to hinder the charging dynamics. We note that the time-dependent detuning induced by the terms $P_n^z(\phi)$ is also present in the two-photon resonance regime. In that setting, however, its impact is relatively weaker, because the additional resonant processes it generates provide a dominant contribution that compensates for the detrimental effect of the time-dependent detuning. This interpretation explains the results obtained when the phase difference is set at $\phi = 0.53\pi$ (two-photon resonance) over a wide range of values of g , and when $\phi = 0.76\pi$ (single-photon resonance) for small g , such as $g = 0.1$, where the charging process is mainly governed by the resonant TLSs. Finally, in the case shown in Fig. 5(d) and Fig. 6(d), where the phase difference is fixed at $\phi = 0.76\pi$ (single-photon resonance) and the coupling is relatively large, $g = 0.3$, off-resonant contributions become important. In particular, even though the system is nominally tuned for single-photon resonance, the relatively large value of g also activates two-photon processes. In this regime, the presence of the terms $P_n^z(\phi)$ improves the efficiency of these processes, so its overall effect becomes beneficial, in contrast to the small g regime where two-photon processes remain marginal. Additional details on the role of the terms $P_n^z(\phi)$ are provided in App. A.

3.1 Single transmission probability

In this section, we compare the analysis discussed above with a simplified effective model in which all N conduction channels of the short hybrid JJ are assumed to share the same transport characteristics. In other words, each channel is characterized by the same effective transmission probability, resulting in a uniform distribution of the ABSs splitting energies. In particular, under this simplified description, we examine the charging protocol discussed earlier and, by comparing with the results of the previous section, we highlight the impact of a non-flat distribution of ABSs splitting energies.

The reason behind this approach lies in the fact that, frequently, in experimental studies of short hybrid JJ devices, ABSs are described by introducing a single effective transmission probability, τ_{eff} , which is extracted by fitting the CPR measured across the junction [75–77]. Similarly, in this study we determine a single effective transmission probability, $\tau_{\text{eff}} \approx 0.93$, by fitting Eq. (2) to the short planar GJJ configuration discussed above, while keeping the same Fermi level $\mu_0 = 6.5\hbar v_F/L$ and junction aspect ratio $W/L = 2$, as in Fig. 2(b).

Within this effective picture, the total Hamiltonian assumes the form of a generalized Dicke model [35, 38, 78]

$$\hat{H}_{\text{gD}} = \hat{H}_{\text{r}} + \varepsilon(\phi) \sum_{n=1}^N \hat{\sigma}_n^z + g(\hat{a} + \hat{a}^\dagger) \mathbf{P} \cdot \sum_{n=1}^N \hat{\boldsymbol{\sigma}}_n + \frac{g^2}{2} (\hat{a} + \hat{a}^\dagger)^2 \mathbf{D} \cdot \sum_{n=1}^N \hat{\boldsymbol{\sigma}}_n, \quad (22)$$

which differs from the bare Dicke Hamiltonian due to the inclusion of a quadratic term in the operator $\hat{a} + \hat{a}^\dagger$ and a linear term in the same operator, $\hat{a} + \hat{a}^\dagger$, which is weighted by $P^z(\phi)$, and commutes with \hat{H}_B . Here, the quantities $\varepsilon(\phi)$, \mathbf{P} , and \mathbf{D} are obtained from Eq. (1) and Eq. (8) by replacing τ_n with τ_{eff} , namely,

$$\varepsilon(\phi) = \Delta_0 \sqrt{1 - \tau_{\text{eff}} \sin^2(\phi/2)}, \quad (23a)$$

$$\mathbf{P} = (P^z(\phi), P^x(\phi))^T = \partial_\phi \varepsilon(\phi) \left(1, -\sqrt{1 - \tau_{\text{eff}}} \tan\left(\frac{\phi}{2}\right) \right)^T, \quad (23b)$$

$$\mathbf{D} = (D^z(\phi), D^x(\phi))^T = \partial_\phi \varepsilon(\phi) \left(\frac{\tau_{\text{eff}} + (2 - \tau_{\text{eff}}) \cos(\phi)}{2 \sin(\phi)}, -\sqrt{1 - \tau_{\text{eff}}} \right)^T. \quad (23c)$$

Analogously to what has been done before, we analyze the time evolution of the energy stored in the QB, measured in units of $N\hbar\omega_r$, under the charging protocol specified in Eq. (9). Here, exploiting the fact that now \hat{S}^2 is a conserved quantity, namely $[\hat{S}^2, \hat{H}_{\text{gD}}(t)] = 0$, we can restrict the computation to a smaller invariant $(N+1) \times (N+1)$ subspace for the ABSs sector, thereby reducing the computational cost required to study the time evolution of the QB system. Moreover, we use as the initial state $|\psi(0)\rangle$, previously defined in Eq. (14), where the matter part $|\downarrow\rangle$ belongs to the Hilbert subspace associated with the maximal eigenvalue of the operator \hat{S}^2 .

Fig. 7 shows the time evolution of the stored energy in the QB system (in units of $N\omega_r$) for the coupling strengths $g = 0.1$ (a) and $g = 0.3$ (b), as a function of the superconducting phase difference ϕ . The specific values $\phi/\pi = 0.82$ (orange dashed line) and $\phi/\pi = 0.48$ (pink dashed line) correspond to the resonance conditions for the single-photon ($2\varepsilon(\phi) = \hbar\omega_r$) and two-photon ($\varepsilon(\phi) = \hbar\omega_r$) processes within the effective model considered, respectively. For $g = 0.1$, the charging efficiency is markedly enhanced at the values of ϕ that correspond to configurations in which all TLSs are tuned in resonance with single- or two-photon processes. Under single-photon resonance, this leads to a maximum stored energy of $E_B^{(g)}(t)/(N\hbar\omega_r) \simeq 86\%$, while under the two-photon resonance, the maximum stored energy reaches $E_B^{(g)}(t)/(N\hbar\omega_r) \simeq 60\%$.

Similarly to the case of a non-flat distribution of energy splittings, for a coupling constant $g = 0.3$, stored energies up to $E_B^{(g)}(t)/(N\hbar\omega_r) \simeq 47\%$ are generally reached at earlier times than for $g = 0.1$, and the larger values are distributed more evenly over broader regions of the density plot. However, the maximum stored energy is obtained when the superconducting phase difference is within the interval $0.7\pi \lesssim \phi \lesssim 0.9\pi$.

Therefore, these results indicate that within this simplified model, for both values of the coupling constant g the charging process is enhanced in those energy configurations where the ABS splitting energy $2\varepsilon(\phi)$ is confined to an energy window centered around $\hbar\omega_r$ (single-photon resonance).

As in the case of a non-flat distribution of TLSs splitting energies, we analyze the impact of the term $P^z(\phi)$. Figs. 8(a)–(c) show the evolution of the stored energy for a fixed value $\phi/\pi = 0.48$, which corresponds to tuning the TLSs to the two-photon resonance, considering the cases $g = 0.1$ and $g = 0.3$, respectively. For both values of g , we observe that the term $P^z(\phi)$ plays a beneficial role in the charging processes, in agreement with the earlier discussion, where we noted that, together with the term $P^x(\phi)$, it introduces additional mechanisms for the creation/disruption of two-photon processes that de-excite/excite a TLS. Figs. 8(b)–(d) show the evolution of the stored energy for a fixed value $\phi/\pi = 0.82$, which corresponds to tuning the TLSs to the single-photon resonance, for the two coupling strengths $g = 0.1$ and $g = 0.3$, respectively. In contrast to the case of a non-flat distribution of TLS splitting energies, we find that, for both values of g , the contribution $P^z(\phi)$ hinders the charging processes. In this case, all TLSs are tuned to satisfy the single-photon resonance condition, and the resulting behavior aligns fully with what is shown in Figs. 6(b)–(d). There, for a non-flat distribution of TLS splitting energies, the blue solid lines select the charging dynamics corresponding to the subgroup of TLSs that are tuned to the single-photon condition.

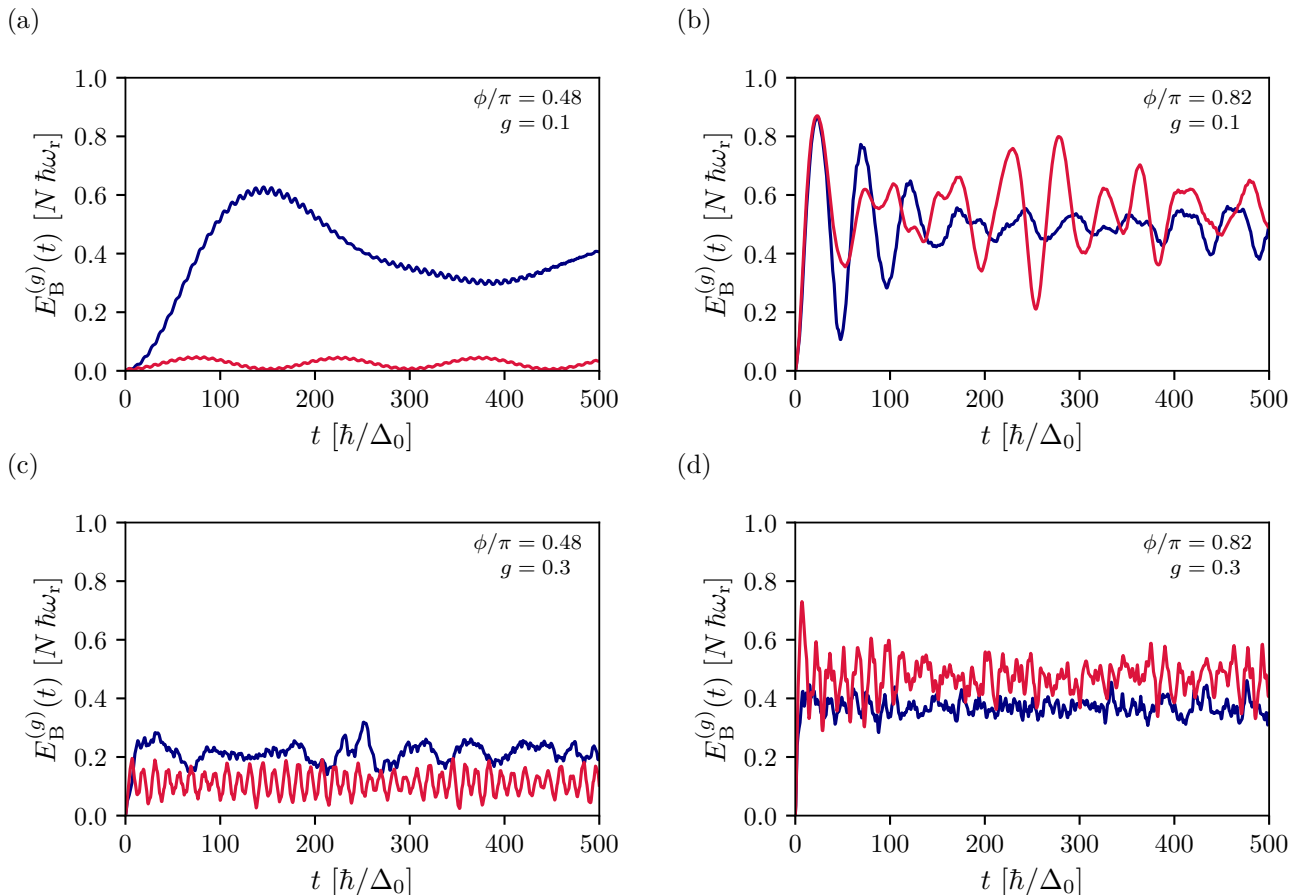


Figure 8: Comparison of time evolution of the energy stored in the QB system (in units of $N\hbar\omega_r$) obtained according to the full Hamiltonian in Eq. (7) (blue solid lines) with the corresponding results computed by neglecting the term $P^z(\phi)$ (red solid lines). We show the results for $\phi/\pi = 0.48$ (a)–(c) and for $\phi/\pi = 0.82$ (b)–(d). In panels (a) and (b) one has $g = 0.1$, while in panels (c) and (d) one has $g = 0.3$. In all panels, the times are reported in units of \hbar/Δ_0 . Other parameters are $\tau_{\text{eff}} = 0.93$, $N = 8$, $\hbar\omega_r = 0.75\Delta_0$.

3.2 Alternative charging protocol: Superconducting phase difference time modulation

Although the protocol in Eq. (9) has been adopted as a reasonable choice in several theoretical studies [37, 79, 80], its actual implementation in scalable architectures remains challenging [46, 81]. As an alternative, we propose a second charging protocol that exploits the dependence of the ABS spectrum on the superconducting phase difference. Here, we assume a sudden quench of the superconductive phase difference across the JJ. This can be obtained by controlling the external magnetic fluxes in cQED setups [82], or by a pulsed voltage drop described as $V(t) = [\hbar\phi/(2e)][\delta(t) - \delta(t - t_c)]$ [83]. Therefore, in the following charging protocol, we implement in Eq. (7) the substitution

$$\phi \rightarrow \bar{\phi}(t) = \phi \Theta(t) \Theta(t_c - t). \quad (24)$$

Here, the applied modulation enables an effective coupling (or decoupling) between the QB and the charger. Unlike approaches based on modulating coupling constants [84–86], the present scheme does not require quantum couplers to actively control interactions between circuit components [87, 88]. This should reduce hardware complexity and may open a promising new direction for the design and investigation of solid-state QBs.

In this alternative charging protocol scenario, before the charging process starts, one has $\phi = 0$ and

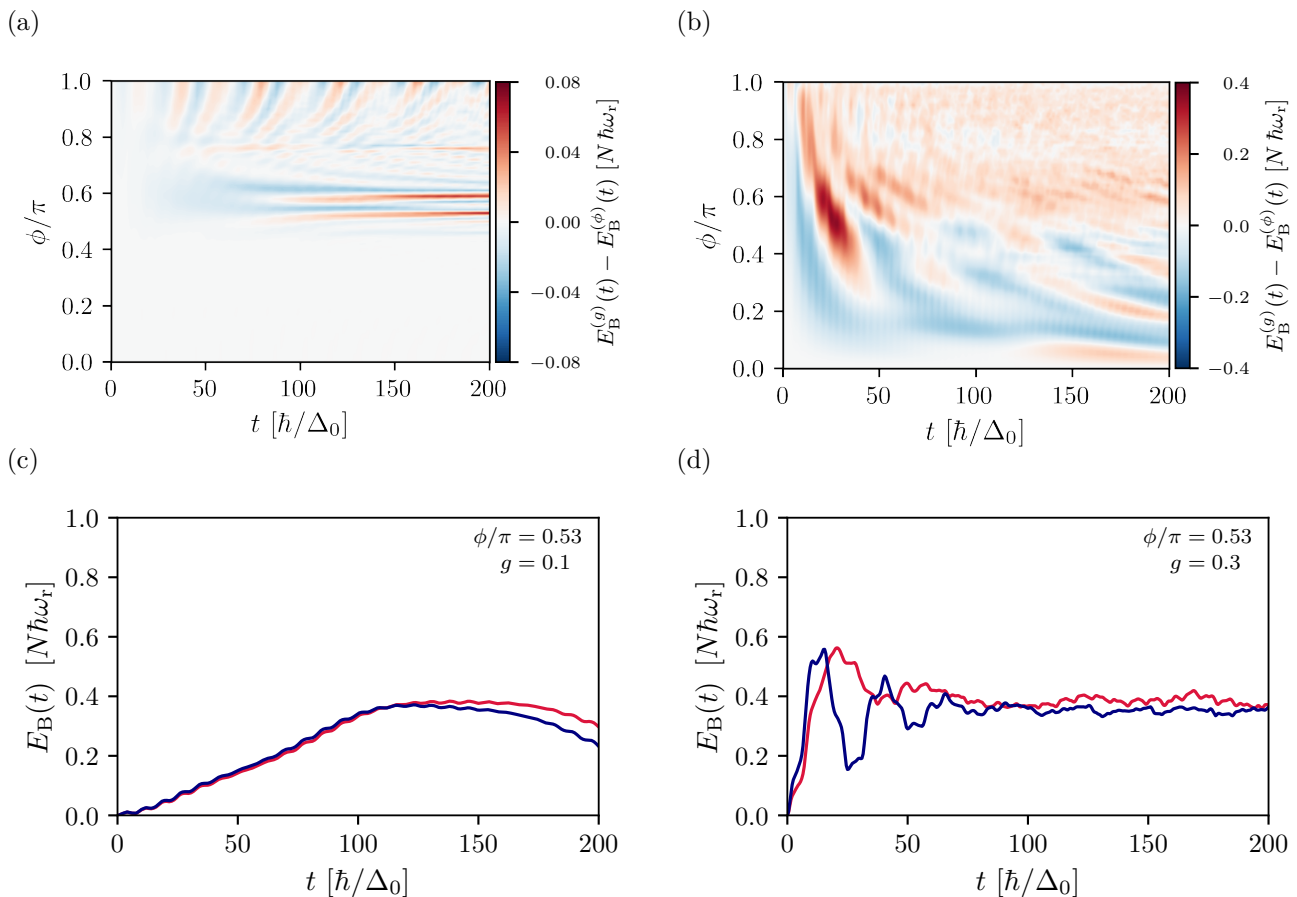


Figure 9: (a)–(b) Time evolution of the difference between the energies stored in the QB system (in units of $N\hbar\omega_r$) by employing the charging protocols in Eq. (9), $E_B^{(g)}$, and Eq. (24), $E_B^{(\phi)}$, respectively. (c)–(d) Comparison of the time evolution of the energy stored in the QB system (in units of $N\hbar\omega_r$), evaluated for $\phi/\pi = 0.53$ (two-photon resonance condition), employing the charging protocols based on coupling strength (red solid line) and based on superconducting phase difference (blue solid line), respectively. (a)–(c) illustrate the case $g = 0.1$, while (b)–(d) the case $g = 0.3$. In all panels, the times are reported in units of \hbar/Δ_0 . Other parameters are $\hbar\omega_r = 0.75\Delta_0$, $\mu_0 = 6.5\hbar v_F/L$ and $W = 2L$.

the total system is described by the initial Hamiltonian

$$\hat{H}_0 = \hbar\omega_r \left(\hat{a}^\dagger \hat{a} + \frac{1}{2} \right) + \Delta_0 \sum_n \hat{\sigma}_n^z + \frac{g^2}{2} (\hat{a} + \hat{a}^\dagger)^2 \left(-\frac{\Delta_0}{4} \sum_n \tau_n \hat{\sigma}_n^z \right). \quad (25)$$

We recall that for the specific case of GJJ, one replaces the label n with the composite index $\nu \equiv (\zeta, m)$. Because the operators $\hat{\sigma}_n^z$ are conserved quantities, i.e., $[\hat{H}_0, \hat{\sigma}_n^z] = 0$, the Hamiltonian in Eq. (25) takes a block-diagonal form when expressed in the common eigenbasis of the set $\{\hat{\sigma}_n^z\}$. If we consider as the initial state a generic factorized eigenstate of all $\hat{\sigma}_n^z$, the time evolution remains confined within the corresponding invariant subspace. Therefore, each operator can be replaced by its eigenvalue $s_n^z = \pm 1$, such that Eq. (25) reduces to an effective quadratic bosonic Hamiltonian parametrized by the initial configuration $\{s_n^z\}$, which reads as follows

$$\hat{H}_0 = \hbar\omega_r \left(\hat{a}^\dagger \hat{a} + \frac{1}{2} \right) + \varepsilon_0 + g_D (\hat{a} + \hat{a}^\dagger)^2, \quad (26)$$

where $\varepsilon_0 = \Delta_0 \sum_n s_n^z$ is the total initial energy of the QB and $g_D = -(g^2 \Delta_0 / 8) \sum_n \tau_n s_n^z$. This Hamiltonian can be brought into diagonal form via a Bogoliubov transformation, resulting in

$$\hat{H}_0 = \hbar\lambda\omega_r \left(\hat{b}^\dagger \hat{b} + \frac{1}{2} \right) + \varepsilon_0, \quad (27)$$

where $\hat{b} = \cosh(x)\hat{a} + \sinh(x)\hat{a}^\dagger$ is a bosonic annihilation operator that acts on a new vacuum state as $\hat{b}|0\rangle_b = 0$, while $x = \ln\sqrt{\lambda}$ with $\lambda = [1 + 4g_D/\hbar\omega_r]^{1/2}$. In complete analogy to Eq. (14), here we consider the following initial state for the charging

$$|\chi_0\rangle = |N\rangle_b \otimes |\downarrow\rangle, \quad (28)$$

where $|N\rangle_b = (1/\sqrt{N!})b^\dagger{}^N|0\rangle_b$ is a Fock state that contains N excitations for the new bosonic mode, while the state $|\downarrow\rangle$ corresponds to the initial configuration $\{s_n^z = -1\}$. By expressing the total Hamiltonian that characterizes the charging process in terms of the new creation (annihilation) operators \hat{b}^\dagger (\hat{b}), we obtain

$$\hat{H} = \hbar\lambda\omega_r \left(\hat{b}^\dagger\hat{b} + \frac{1}{2} \right) + \sum_{n=1}^N \varepsilon_n(\phi) \hat{\sigma}_n^z + g_\lambda(\hat{b} + \hat{b}^\dagger) \sum_{n=1}^N \mathbf{P}_n \cdot \hat{\boldsymbol{\sigma}}_n + \frac{g_\lambda^2}{2} (\hat{b} + \hat{b}^\dagger)^2 \sum_{n=1}^N (\mathbf{D}_n \cdot \hat{\boldsymbol{\sigma}}_n + D_{0,n}^z), \quad (29)$$

where $g_\lambda = g\sqrt{\lambda}$ is the renormalized coupling constant and $D_{0,n}^z = D_n^z|_{\phi=0}$.

Figs. 9(a)-(b) show how the quantity $E_B^{(g)} - E_B^{(\phi)}$, i.e., the difference between the energy stored in the QB system using the coupling strength protocol and that obtained with the superconducting phase-difference protocol, evolves for continuous values of ϕ , for two coupling strengths, $g = 0.1$ and $g = 0.3$, respectively. For $g = 0.1$, the charging performances of the two protocols are nearly indistinguishable. Indeed, the difference between them remains relatively small, staying below $0.1N\hbar\omega_r$. This confirms that the two protocols also yield comparable results under the two-photon resonance condition $\phi/\pi = 0.53$, discussed in the previous sections. Within this coupling regime, Fig. 9(c) shows the stored energy calculated at $\phi/\pi = 0.53$, using the charging protocols based on the coupling strength $E_B^{(g)}$ (solid red line) and the phase difference $E_B^{(\phi)}$ (solid blue line), respectively. The two resulting curves exhibit very similar behavior with comparable maximum values of the stored energy. For this particular choice of microscopic parameters, their differences become appreciable only at longer times. Conversely, for the case $g = 0.3$ shown in Fig. 9(b), the discrepancy between the two protocols becomes more pronounced, up to $0.4N\hbar\omega_r$ in a region around the two-photon resonance condition. At $\phi/\pi = 0.53$, corresponding to the two-photon resonance condition, Fig. 9(d) shows that the time evolution of the stored energy for the coupling-strength protocol (red solid line) and the phase-difference protocol (blue solid line) is already distinguishable at early times. However, for this value of the coupling constant, the maximum stored energy reached in the two protocols is comparable. Notably, the phase-difference protocol exhibits faster oscillations of the stored energy during the initial stage of the dynamics.

Given that both protocols are characterized by a comparable stored energy, particularly in the small coupling regime, and allow for an efficient exploitation of two-photon processes compared with single-photon ones, the selection between them can primarily rely on considerations dictated by practical implementation and experimental constraints.

4 Conclusions

In this work, we investigated the possible implementation of a Dicke-like QB based on a superconducting circuit architecture. The setup features an LC resonator that is inductively coupled to a superconducting loop containing a two-dimensional superconductor–semiconductor JJ. Focusing on the case of a finite-width GJJ in the short-junction limit, we described the ABSs within the link, each associated with a transport channel, as an ensemble of TLSs coupled with the photons into the resonator.

First, we examined the charging performance of this device using a standard protocol that is based on the energy transfer from the photons to the TLSs via a sudden change of the inductive coupling strength. In the weak-coupling regime, our findings indicate that when the system is tuned in such a way that a number of TLSs satisfy a two-photon resonance condition, the charging process is improved with respect to the cases where the single-photon resonance is achieved.

This behavior is due to the presence of a longitudinal linear coupling term in the interaction Hamiltonian, which originates microscopically from the coupling between the LC flux and the supercurrent passing through the junction. Our analysis showed that this term, which is absent in the conventional Dicke model, can generate additional two-photon resonant processes that assist the charging dynamics.

These conclusions were further corroborated by comparison with an effective model in which all the TLSs composing the QB have the same energy splittings.

Finally, we introduced an alternative charging protocol based on the sensitivity of the ABSs spectrum with respect to the superconducting phase difference. Notably, when this phase difference is abruptly changed through a sudden quench, the resulting energy storage behavior resembles that obtained with the coupling-based protocol, highlighting how the flexibility of this platform can adapt to possible experimental limitations.

To conclude, our theoretical analysis shows that the proposed device can serve as an efficient and versatile implementation of a solid-state QB, laying the groundwork for future experimental developments in the field.

A Effect of longitudinal terms, linear in the coupling constant, on the charging process

In this appendix, we provide a further analysis of the role played by the contribution of the longitudinal terms $P_n^z(\phi)$, which enter as first-order terms in g in Eq. (7). In particular, Fig. A.1 combines what is shown in Fig. 5 and Fig. 6 of the main text. Here, the energy stored in the QB, $E^{(g)}(t)$ (in units of $N\hbar\omega_r$), calculated by omitting the terms $P_n^z(\phi)$ in Eq. (7), is split into a close to resonance (green solid line) and an off-resonant part (black solid lines), as specified in Eqs. (17). For comparison, we also show the time evolution of the stored energy in the QB system when the terms $P_n^z(\phi)$ are taken into account, again separated into a close to resonance contribution (blue solid lines) and an off-resonant contribution (red solid lines), as already shown in Fig. 6.

In each panel, we distinguish between the contributions due to TLSs that belong to the set \mathcal{S} (blue and green lines) and those that do not (red and black lines) according to the criteria introduced in the main text. For the case $\phi = 0.53$, close to the two-photon resonance, shown in Fig. A.1(a)–(c), this set is defined as $\mathcal{S} \equiv \{\nu = \pm 3, \pm 4\}$ (see Fig. 2(b) for comparison). Conversely, for $\phi = 0.76$, close to the single-photon resonance, shown in Fig. A.1(b)–(d), the corresponding set is $\mathcal{S} \equiv \{\nu = \pm 1, \pm 2\}$.

Specifically, Fig. A.1(a) shows the case $g = 0.1$ with the phase difference set at $\phi/\pi = 0.53$. As discussed in the main text, under these conditions, the charging process is expected to be dominated primarily by two-photon resonant processes. From the comparison between the curves in Fig. A.1(a) it is evident that the terms $P_n^z(\phi)$ enhance the energy exclusively close to resonance, namely for the TLSs characterized by $|2\hbar\omega_r - 2\varepsilon_n(\phi)| < \Delta_0/10$. Moreover, in Fig. A.1(c), we keep the same phase difference but increase the coupling constant to $g = 0.3$. We again find that the terms $P_n^z(\phi)$ act as supporting contributions that specifically affect the TLSs belonging to \mathcal{S} . For both values of the coupling constant, the contributions for TLSs outside the set \mathcal{S} are negligible.

Figs. A.1(b)–(d) refer to the single-photon resonance condition ($\phi/\pi = 0.76$). In particular, Fig. A.1(b) shows the case with $g = 0.1$. Here, there is a subset of TLSs, again denoted by \mathcal{S} , which satisfies $|\hbar\omega_r - 2\varepsilon_n(\phi)| < \Delta_0/10$. According to the perturbative analysis presented in the main text (see Eq. (19) and Eq. (21)), the charging dynamics is therefore expected to be predominantly governed by single-photon resonant processes. However, for $\phi/\pi = 0.76$, contributions from states outside \mathcal{S} (red solid line) produce a small but noticeable contribution. This is because their effective transverse coupling $g|P_n^x\phi|$ is larger than that of ABSs within \mathcal{S} , which is, in turn, related to their transmission probabilities.

In this regime, we recall that the terms $P_n^z(\phi)$ act as a source of disturbance affecting the energy contribution of the resonant TLSs (solid blue line) belonging to \mathcal{S} . In fact, when the terms $P_n^z(\phi)$ are removed from the Hamiltonian, the stored energy increases (solid green line). Keeping the same phase difference but increasing the coupling constant to $g = 0.3$, Fig. A.1(d) shows that the influence of the terms $P_n^z(\phi)$ results in a slightly enhanced overall contribution. This behavior can be interpreted as the outcome of a compensation between two competing effects. The contribution from two-photon off-resonant contributions increases, primarily due to the larger coupling constant, as indicated by the change from the black solid line to the red solid line. However, similar to what is illustrated in Fig. A.1(b), the terms $P_n^z(\phi)$ also lead to a suppression of the contribution associated with the single-photon resonant contributions. This is demonstrated by the difference between the green solid line and

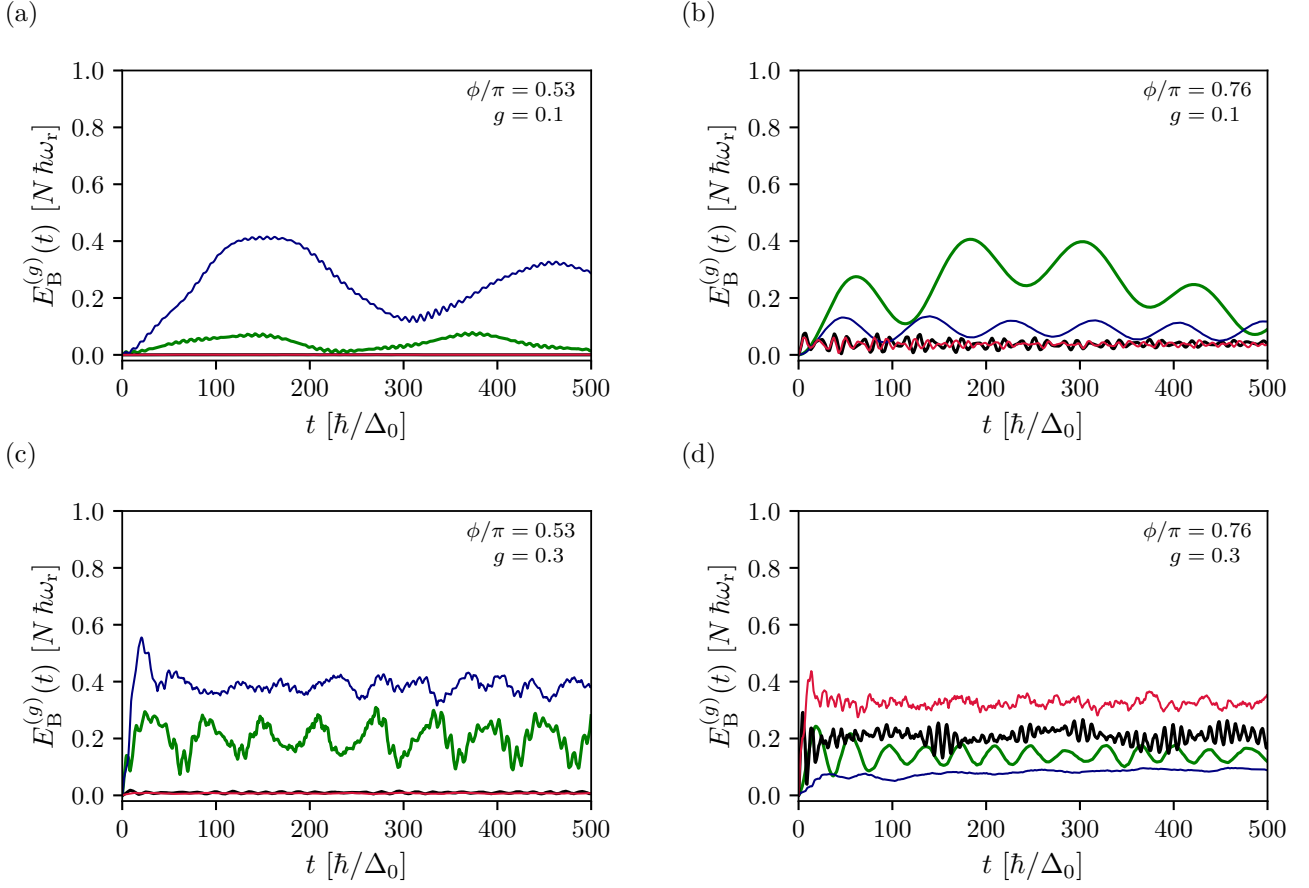


Figure A.1: Time evolution of the stored energy in the QB system (in units of $N\hbar\omega_r$), computed by neglecting the terms $P_n^z(\phi)$ in Eq. (7), and decomposed into a close resonant component (green solid line) and an off-resonant component (black solid lines), as given by Eq. (17). As a guide eye, we also show the time evolution of the stored energy in the QB system when the terms $P_n^z(\phi)$ are included, again split into a resonant contribution (blue solid lines) and an off-resonant contribution (red solid lines), already presented in Fig. 6. Panels (a)–(c) correspond to $\phi/\pi = 0.53$, where the set of close resonant TLSs is $\mathcal{S} \equiv \{\nu = \pm 3, \pm 4\}$. Whereas, (b)–(d) show the case $\phi/\pi = 0.76$, for which the close resonant TLSs set is $\mathcal{S} \equiv \{\nu = \pm 1, \pm 2\}$. Panels (a)–(b) correspond to coupling strength $g = 0.1$, while (c)–(d) refer to $g = 0.3$. In all panels, time is expressed in units of \hbar/Δ_0 . The remaining parameters are $\hbar\omega_r = 0.75\Delta_0$, $\mu_0 = 6.5\hbar v_F/L$, and $W = 2L$.

the blue solid line.

Acknowledgments

G.G., F.M.D.P., and D.F. acknowledge support from the project PRIN 2022 – 2022XK5CPX (PE3) SoS-QuBa – “Solid State Quantum Batteries: Characterization and Optimization” funded within the programme “PNRR Missione 4 - Componente 2 - Investimento 1.1 Fondo per il Programma Nazionale di Ricerca e Progetti di Rilevante Interesse Nazionale (PRIN)”, funded by the European Union – Next Generation EU. V.V. and E.P. are thankful for the PNRR MUR project PE0000023-NQSTI. E.P. acknowledges support from COST Action CA21144 SuperQuMap, and Università degli Studi di Catania, project TCMQI PIACERI 2024/2026.

References

- [1] J.Q. Quach, G. Cerullo, and T. Virgili. Quantum batteries: The future of energy storage? *Joule*, 7(10):2195–2200, 2023.
- [2] Francesco Campaioli, Stefano Gherardini, James Q. Quach, Marco Polini, and Gian Marcello Andolina. Colloquium: Quantum batteries. *Rev. Mod. Phys.*, 96:031001, Jul 2024.
- [3] Andrea Camposeo, Tersilla Virgili, Floriana Lombardi, Giulio Cerullo, Dario Pisignano, and Marco Polini. Quantum Batteries: A Materials Science Perspective. *Advanced Materials*, 37(17):2415073, 2025.
- [4] Dario Ferraro, Fabio Cavaliere, Marco G. Genoni, Giuliano Benenti, and Maura Sassetti. Opportunities and challenges of quantum batteries. *Nature Reviews Physics*, 8(2):115–127, Feb 2026.
- [5] WANG Lu, WU Fenglin, LI Nana, GUO Senyan, FAN Hao, LIU Shuqian, and LIU Siyuan. Research progress of quantum battery. *Acta Physica Sinica*, 75(4), 2026.
- [6] Olivier Ezratty. Understanding Quantum Technologies 2025, 2025.
- [7] Alexia Auffèves. Quantum Technologies Need a Quantum Energy Initiative. *PRX Quantum*, 3:020101, Jun 2022.
- [8] Giulio Chiribella, Yuxiang Yang, and Renato Renner. Fundamental Energy Requirement of Reversible Quantum Operations. *Phys. Rev. X*, 11:021014, Apr 2021.
- [9] Yaniv Kurman, Kieran Hymas, Arkady Fedorov, William J. Munro, and James Quach. Powering Quantum Computation with Quantum Batteries. *Phys. Rev. X*, 16:011016, Jan 2026.
- [10] Robert Alicki and Mark Fannes. Entanglement boost for extractable work from ensembles of quantum batteries. *Phys. Rev. E*, 87:042123, Apr 2013.
- [11] Felix C Binder, Sai Vinjanampathy, Kavan Modi, and John Goold. Quantacell: powerful charging of quantum batteries. *New Journal of Physics*, 17(7):075015, jul 2015.
- [12] Thao P. Le, Jesper Levinsen, Kavan Modi, Meera M. Parish, and Felix A. Pollock. Spin-chain model of a many-body quantum battery. *Phys. Rev. A*, 97:022106, Feb 2018.
- [13] Davide Rossini, Gian Marcello Andolina, and Marco Polini. Many-body localized quantum batteries. *Phys. Rev. B*, 100:115142, Sep 2019.
- [14] Felipe Barra, Karen V Hovhannisyán, and Alberto Imparato. Quantum batteries at the verge of a phase transition. *New Journal of Physics*, 24(1):015003, jan 2022.
- [15] Riccardo Grazi, Daniel Sacco Shaikh, Maura Sassetti, Niccoló Traverso Ziani, and Dario Ferraro. Controlling Energy Storage Crossing Quantum Phase Transitions in an Integrable Spin Quantum Battery. *Phys. Rev. Lett.*, 133:197001, Nov 2024.
- [16] A.G. Catalano, S.M. Giampaolo, O. Morsch, V. Giovannetti, and F. Franchini. Frustrating Quantum Batteries. *PRX Quantum*, 5:030319, Jul 2024.
- [17] Riccardo Grazi, Fabio Cavaliere, Maura Sassetti, Dario Ferraro, and Niccolò Traverso Ziani. Charging free fermion quantum batteries. *Chaos, Solitons & Fractals*, 196:116383, 2025.
- [18] Zhi-Guang Lu, Guoqing Tian, Xin-You Lü, and Cheng Shang. Topological Quantum Batteries. *Phys. Rev. Lett.*, 134:180401, May 2025.
- [19] Le Bin Ho, Duc Tuan Hoang, Tran Duong Anh-Tai, Thomas Busch, and Thomás Fogarty. Boosting the Performance of a Lipkin-Meshkov-Glick Quantum Battery via Symmetry-Breaking Quenches and Bosonic Baths, 2026.

- [20] Jitendra Joshi and T. S. Mahesh. Experimental investigation of a quantum battery using star-topology NMR spin systems. *Phys. Rev. A*, 106:042601, Oct 2022.
- [21] Clebson Cruz, Maron F Anka, Mario S Reis, Romain Bachelard, and Alan C Santos. Quantum battery based on quantum discord at room temperature. *Quantum Science and Technology*, 7(2):025020, mar 2022.
- [22] Stella Seah, Martí Perarnau-Llobet, Géraldine Haack, Nicolas Brunner, and Stefan Nimmrichter. Quantum Speed-Up in Collisional Battery Charging. *Phys. Rev. Lett.*, 127:100601, Aug 2021.
- [23] Vahid Shaghaghi, Varinder Singh, Giuliano Benenti, and Dario Rosa. Micromasers as quantum batteries. *Quantum Science and Technology*, 7(4):04LT01, aug 2022.
- [24] Vahid Shaghaghi, Varinder Singh, Matteo Carrega, Dario Rosa, and Giuliano Benenti. Lossy Micromaser Battery: Almost Pure States in the Jaynes–Cummings Regime. *Entropy*, 25(3), 2023.
- [25] Daniele Morrone, Matteo A C Rossi, Andrea Smirne, and Marco G Genoni. Charging a quantum battery in a non-Markovian environment: a collisional model approach. *Quantum Science and Technology*, 8(3):035007, may 2023.
- [26] Nicolò Massa, Fabio Cavaliere, and Dario Ferraro. The Collisional Charging of a Transmon Quantum Battery. *Batteries*, 11(7), 2025.
- [27] Seyed Navid Elyasi, Matteo A C Rossi, and Marco G Genoni. Experimental simulation of daemonic work extraction in open quantum batteries on a digital quantum computer. *Quantum Science and Technology*, 10(2):025017, feb 2025.
- [28] Chang-Kang Hu, Jiawei Qiu, Paulo J P Souza, Jiahao Yuan, Yuxuan Zhou, Libo Zhang, Ji Chu, Xianchuang Pan, Ling Hu, Jian Li, Yuan Xu, Youpeng Zhong, Song Liu, Fei Yan, Dian Tan, R Bachelard, C J Villas-Boas, Alan C Santos, and Dapeng Yu. Optimal charging of a superconducting quantum battery. *Quantum Science and Technology*, 7(4):045018, aug 2022.
- [29] Giulia Gemme, Michele Grossi, Sofia Vallecorsa, Maura Sassetti, and Dario Ferraro. Qutrit quantum battery: Comparing different charging protocols. *Phys. Rev. Res.*, 6:023091, Apr 2024.
- [30] Luca Razzoli, Giulia Gemme, Iliia Khomchenko, Maura Sassetti, Henni Ouerdane, Dario Ferraro, and Giuliano Benenti. Cyclic solid-state quantum battery: thermodynamic characterization and quantum hardware simulation. *Quantum Science and Technology*, 10(1):015064, jan 2025.
- [31] Li Li, Si-Lu Zhao, Yun-Hao Shi, Bing-Jie Chen, Xinhui Ruan, Gui-Han Liang, Wei-Ping Yuan, Jia-Cheng Song, Cheng-Lin Deng, Yu Liu, Tian-Ming Li, Zheng-He Liu, Xue-Yi Guo, Xiaohui Song, Kai Xu, Heng Fan, Zhongcheng Xiang, and Dongning Zheng. Stable and efficient charging of superconducting capacitively shunted flux quantum batteries. *Phys. Rev. Appl.*, 24:054033, Nov 2025.
- [32] Karen V. Hovhannisyanyan, Felipe Barra, and Alberto Imparato. Charging assisted by thermalization. *Phys. Rev. Res.*, 2:033413, Sep 2020.
- [33] Fabio Cavaliere, Giulia Gemme, Giuliano Benenti, Dario Ferraro, and Maura Sassetti. Dynamical blockade of a reservoir for optimal performances of a quantum battery. *Communications Physics*, 8(1):76, 2025.
- [34] F. Cavaliere, D. Ferraro, M. Carrega, G. Benenti, and M. Sassetti. Quantum advantage bounds for a multipartite Gaussian battery, 2025.
- [35] R. H. Dicke. Coherence in Spontaneous Radiation Processes. *Phys. Rev.*, 93:99–110, Jan 1954.
- [36] Peter Kirton, M. M. Roses, Jonathan Keeling, and E. G. Dalla Torre. Introduction to the Dicke Model: From Equilibrium to Nonequilibrium, and Vice Versa. *Advanced Quantum Technologies*, 2(1-2):1800043, 2019.

- [37] Dario Ferraro, Michele Campisi, Gian Marcello Andolina, Vittorio Pellegrini, and Marco Polini. High-Power Collective Charging of a Solid-State Quantum Battery. *Phys. Rev. Lett.*, 120:117702, Mar 2018.
- [38] Alba Crescente, Matteo Carrega, Maura Sassetti, and Dario Ferraro. Ultrafast charging in a two-photon Dicke quantum battery. *Phys. Rev. B*, 102:245407, Dec 2020.
- [39] Dario Ferraro, Gian Marcello Andolina, Michele Campisi, Vittorio Pellegrini, and Marco Polini. Quantum supercapacitors. *Phys. Rev. B*, 100:075433, Aug 2019.
- [40] Javier Carrasco, Jerónimo R. Maze, Carla Hermann-Avigliano, and Felipe Barra. Collective enhancement in dissipative quantum batteries. *Phys. Rev. E*, 105:064119, Jun 2022.
- [41] Giulia Gemme, Gian Marcello Andolina, Francesco Maria Dimitri Pellegrino, Maura Sassetti, and Dario Ferraro. Off-Resonant Dicke Quantum Battery: Charging by Virtual Photons. *Batteries*, 9(4), 2023.
- [42] Dong-Lin Yang, Fang-Mei Yang, and Fu-Quan Dou. Three-level Dicke quantum battery. *Phys. Rev. B*, 109:235432, Jun 2024.
- [43] Harsh Sharma and Himadri Shekhar Dhar. Quadratic power enhancement in extended Dicke quantum battery, 2025.
- [44] Gian Marcello Andolina, Maximilian Keck, Andrea Mari, Vittorio Giovannetti, and Marco Polini. Quantum versus classical many-body batteries. *Phys. Rev. B*, 99:205437, May 2019.
- [45] Sergi Julià-Farré, Tymoteusz Salamon, Arnau Riera, Manabendra N. Bera, and Maciej Lewenstein. Bounds on the capacity and power of quantum batteries. *Phys. Rev. Res.*, 2:023113, May 2020.
- [46] James Q. Quach, Kirsty E. McGhee, Lucia Ganzer, Dominic M. Rouse, Brendon W. Lovett, Erik M. Gauger, Jonathan Keeling, Giulio Cerullo, David G. Lidzey, and Tersilla Virgili. Superabsorption in an organic microcavity: Toward a quantum battery. *Science Advances*, 8(2):eabk3160, 2022.
- [47] Carla Rodríguez, Dario Rosa, and Jan Olle. Artificial intelligence discovery of a charging protocol in a micromaser quantum battery. *Phys. Rev. A*, 108:042618, Oct 2023.
- [48] Paolo Andrea Erdman, Gian Marcello Andolina, Vittorio Giovannetti, and Frank Noé. Reinforcement Learning Optimization of the Charging of a Dicke Quantum Battery. *Phys. Rev. Lett.*, 133:243602, Dec 2024.
- [49] Peng-Yu Sun, Hang Zhou, and Fu-Quan Dou. Cavity-Heisenberg spin-j chain quantum battery and reinforcement learning optimization. *New Journal of Physics*, 27(12):124513, dec 2025.
- [50] Daniel J. Tibben, Enrico Della Gaspera, Joel van Embden, Philipp Reineck, James Q. Quach, Francesco Campaioli, and Daniel E. Gómez. Extending the Self-Discharge Time of Dicke Quantum Batteries Using Molecular Triplets. *PRX Energy*, 4:023012, Jun 2025.
- [51] Kieran Hymas, Jack B. Muir, Daniel Tibben, Joel van Embden, Tadahiko Hirai, Christopher J. Dunn, Daniel E. Gómez, James A. Hutchison, Trevor A. Smith, and James Q. Quach. Superextensive electrical power from a quantum battery. *Light: Science & Applications*, 15(1):168, Mar 2026.
- [52] Ze-Liang Xiang, Sahel Ashhab, J. Q. You, and Franco Nori. Hybrid quantum circuits: Superconducting circuits interacting with other quantum systems. *Rev. Mod. Phys.*, 85:623–653, Apr 2013.
- [53] P. Krantz, M. Kjaergaard, F. Yan, T. P. Orlando, S. Gustavsson, and W. D. Oliver. A quantum engineer’s guide to superconducting qubits. *Applied Physics Reviews*, 6(2):021318, 06 2019.
- [54] C. W. J. Beenakker and H. van Houten. Josephson current through a superconducting quantum point contact shorter than the coherence length. *Phys. Rev. Lett.*, 66:3056–3059, Jun 1991.

- [55] A. Zazunov, V. S. Shumeiko, G. Wendin, and E. N. Bratus'. Dynamics and phonon-induced decoherence of Andreev level qubit. *Phys. Rev. B*, 71:214505, Jun 2005.
- [56] C. W. J. Beenakker. *Three "Universal" Mesoscopic Josephson Effects*, page 235–253. Springer Berlin Heidelberg, 1992.
- [57] C. Janvier, L. Tosi, L. Bretheau, undefined. Ö. Girit, M. Stern, P. Bertet, P. Joyez, D. Vion, D. Esteve, M. F. Goffman, H. Pothier, and C. Urbina. Coherent manipulation of Andreev states in superconducting atomic contacts. *Science*, 349(6253):1199–1202, September 2015.
- [58] Landry Bretheau. *Localized Excitations in Superconducting Atomic Contacts: probing the Andreev doublet*. Phd thesis, Ecole Polytechnique, February 2013.
- [59] Francesco M. D. Pellegrino, Giuseppe Falci, and Elisabetta Paladino. Effect of dilute impurities on short graphene Josephson junctions. *Communications Physics*, 5(1):265, October 2022.
- [60] Uri Vool and Michel Devoret. Introduction to quantum electromagnetic circuits. *International Journal of Circuit Theory and Applications*, 45(7):897–934, 2017.
- [61] Sunghun Park, C. Metzger, L. Tosi, M. F. Goffman, C. Urbina, H. Pothier, and A. Levy Yeyati. From Adiabatic to Dispersive Readout of Quantum Circuits. *Phys. Rev. Lett.*, 125:077701, Aug 2020.
- [62] M. Hays, V. Fatemi, K. Serniak, D. Bouman, S. Diamond, G. de Lange, P. Krogstrup, J. Nygård, A. Geresdi, and M. H. Devoret. Continuous monitoring of a trapped superconducting spin. *Nature Physics*, 16(11):1103–1107, July 2020.
- [63] C. Metzger, Sunghun Park, L. Tosi, C. Janvier, A. A. Reynoso, M. F. Goffman, C. Urbina, A. Levy Yeyati, and H. Pothier. Circuit-QED with phase-biased Josephson weak links. *Phys. Rev. Research*, 3:013036, Jan 2021.
- [64] V. Varrica, G. Falci, E. Paladino, and F. M. D. Pellegrino. Hybrid light-matter excitations and spontaneous time-reversal symmetry breaking in two-dimensional Josephson Junctions. 2026.
- [65] S. Felicetti, J. S. Pedernales, I. L. Egusquiza, G. Romero, L. Lamata, D. Braak, and E. Solano. Spectral collapse via two-phonon interactions in trapped ions. *Phys. Rev. A*, 92:033817, Sep 2015.
- [66] S. Felicetti, D. Z. Rossatto, E. Rico, E. Solano, and P. Forn-Díaz. Two-photon quantum Rabi model with superconducting circuits. *Phys. Rev. A*, 97:013851, Jan 2018.
- [67] Pierre Nataf and Cristiano Ciuti. No-go theorem for superradiant quantum phase transitions in cavity QED and counter-example in circuit QED. *Nature Communications*, 1(1):72, Sep 2010.
- [68] G. M. Andolina, F. M. D. Pellegrino, V. Giovannetti, A. H. MacDonald, and M. Polini. Cavity quantum electrodynamics of strongly correlated electron systems: A no-go theorem for photon condensation. *Phys. Rev. B*, 100:121109(R), Sep 2019.
- [69] Gian Marcello Andolina, Donato Farina, Andrea Mari, Vittorio Pellegrini, Vittorio Giovannetti, and Marco Polini. Charger-mediated energy transfer in exactly solvable models for quantum batteries. *Phys. Rev. B*, 98:205423, Nov 2018.
- [70] Christoph Sträter, Oleksandr Tsyplatyev, and Alexandre Faribault. Nonequilibrium dynamics in the strongly excited inhomogeneous Dicke model. *Phys. Rev. B*, 86:195101, Nov 2012.
- [71] I. Diniz, S. Portolan, R. Ferreira, J. M. Gérard, P. Bertet, and A. Auffèves. Strongly coupling a cavity to inhomogeneous ensembles of emitters: Potential for long-lived solid-state quantum memories. *Phys. Rev. A*, 84:063810, Dec 2011.
- [72] Oleksandr Tsyplatyev and Daniel Loss. Dynamics of the inhomogeneous Dicke model for a single-boson mode coupled to a bath of nonidentical spin-1/2 systems. *Phys. Rev. A*, 80:023803, Aug 2009.

- [73] M. Titov and C. W. J. Beenakker. Josephson effect in ballistic graphene. *Phys. Rev. B*, 74:041401(R), Jul 2006.
- [74] Jun John Sakurai. *Modern Quantum Mechanics*. Addison-Wesley, Reading, MA, 1994.
- [75] F. Nichele, E. Portolés, A. Fornieri, A. M. Whiticar, A. C. C. Drachmann, S. Gronin, T. Wang, G. C. Gardner, C. Thomas, A. T. Hatke, M. J. Manfra, and C. M. Marcus. Relating Andreev bound states and supercurrents in hybrid Josephson junctions. *Phys. Rev. Lett.*, 124:226801, Jun 2020.
- [76] A. Iorio, A. Crippa, B. Turini, S. Salimian, M. Carrega, L. Chirolli, V. Zannier, L. Sorba, E. Strambini, F. Giazotto, and S. Heun. Half-integer Shapiro steps in highly transmissive InSb nanoflag Josephson junctions. *Phys. Rev. Res.*, 5:033015, Jul 2023.
- [77] M. Hinderling, S. C. ten Kate, M. Coraiola, D.Z. Haxell, M. Stiefel, M. Mergenthaler, S. Paredes, S.W. Bedell, D. Sabonis, and F. Nichele. Direct Microwave Spectroscopy of Andreev Bound States in Planar Ge Josephson Junctions. *PRX Quantum*, 5:030357, Sep 2024.
- [78] F. M. D. Pellegrino, L. Chirolli, Rosario Fazio, V. Giovannetti, and Marco Polini. Theory of integer quantum Hall polaritons in graphene. *Phys. Rev. B*, 89:165406, Apr 2014.
- [79] Gian Marcello Andolina, Maximilian Keck, Andrea Mari, Michele Campisi, Vittorio Giovannetti, and Marco Polini. Extractable Work, the Role of Correlations, and Asymptotic Freedom in Quantum Batteries. *Phys. Rev. Lett.*, 122:047702, Feb 2019.
- [80] Luca Razzoli, Giulia Gemme, Iliia Khomchenko, Maura Sassetti, Henni Ouerdane, Dario Ferraro, and Giuliano Benenti. Cyclic solid-state quantum battery: thermodynamic characterization and quantum hardware simulation. *Quantum Science and Technology*, 10(1):015064, Jan 2025.
- [81] Samira Elghaayda, Asad Ali, Saif Al-Kuwari, Artur Czerwinski, Mostafa Mansour, and Saeed Haddadi. Performance of a Superconducting Quantum Battery. *Advanced Quantum Technologies*, March 2025.
- [82] Jacob Bryon, D.K. Weiss, Xinyuan You, Sara Sussman, Xanthe Croot, Ziwen Huang, Jens Koch, and Andrew A. Houck. Time-Dependent Magnetic Flux in Devices for Circuit Quantum Electrodynamics. *Phys. Rev. Appl.*, 19:034031, Mar 2023.
- [83] Juan Jose Garcia-Ripoll. *Quantum Information and Quantum Optics with Superconducting Circuits*. Cambridge University Press, 2022.
- [84] Eyob A. Sete, Angela Q. Chen, Riccardo Manenti, Shobhan Kulshreshtha, and Stefano Poletto. Floating Tunable Coupler for Scalable Quantum Computing Architectures. *Phys. Rev. Appl.*, 15:064063, Jun 2021.
- [85] Daniel L. Campbell, Archana Kamal, Leonardo Ranzani, Michael Senatore, and Matthew D. LaHaye. Modular Tunable Coupler for Superconducting Circuits. *Phys. Rev. Appl.*, 19:064043, Jun 2023.
- [86] Lukas Heunisch, Christopher Eichler, and Michael J. Hartmann. Tunable coupler to fully decouple and maximally localize superconducting qubits. *Phys. Rev. Appl.*, 20:064037, Dec 2023.
- [87] R. Haller, G. Fülöp, D. Indolese, J. Ridderbos, R. Kraft, L. Y. Cheung, J. H. Ungerer, K. Watanabe, T. Taniguchi, D. Beckmann, R. Danneau, P. Virtanen, and C. Schönenberger. Phase-dependent microwave response of a graphene Josephson junction. *Phys. Rev. Res.*, 4:013198, Mar 2022.
- [88] David Monroe, Chenghao Shen, Dario Tringali, Mohammad Alidoust, Tong Zhou, and Igor Žutić. Phase jumps in Josephson junctions with time-dependent spin-orbit coupling. *Applied Physics Letters*, 125(1), July 2024.